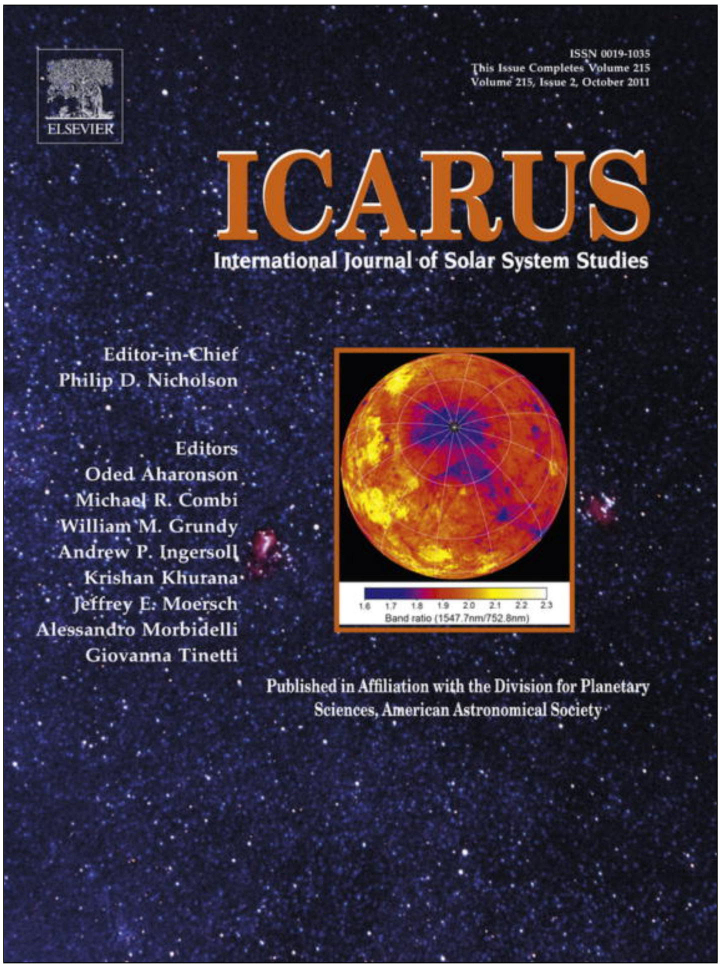
ISSN 0019-1035
This Issue Completes Volume 215
Volume 215, Issue 2, October 2011
ELSEVIER
ICARUS
International Journal of Solar System Studies
Editor-in-Chief
Philip D. Nicholson
Editors
Oded Aharonson
Michael R. Combi
William M. Grundy
Andrew P. Ingersoll
Krishan Khurana
Jeffrey E. Moersch
Alessandro Morbidelli
Giovanna Tinetti
Band ratio (1547.7nm/752.8nm)
Published in Affiliation with the Division for Planetary Sciences, American Astronomical Society

Icarus 215 (2011) 695–711

Contents lists available at ScienceDirect

Icarus

journal homepage: www.elsevier.com/locate/icarus

The Christiansen Effect in Saturn's narrow dusty rings and the spectral identification of clumps in the F ring

M.M. Hedman [a,*], P.D. Nicholson [a], M.R. Showalter [b], R.H. Brown [c], B.J. Buratti [d], R.N. Clark [e], K. Baines [d], C. Sotin [d]

[a] Department of Astronomy, Cornell University, Ithaca, NY 14853, United States
[b] SETI Institute, Mountain View, CA 94043, United States
[c] Lunar and Planetary Laboratory, University of Arizona, Tuscon, AZ 85721, United States
[d] Jet Propulsion Laboratory, 4800 Oak Grove Drive, Pasadena, CA 91109, United States
[e] USGS, Mail Stop 964, PO Box 25046, Federal Center, Denver, CO 80225, United States

ARTICLE INFO

Article history:
Available online 6 March 2011

Keywords:
Planetary rings
Saturn, Rings
Spectroscopy

ABSTRACT

Stellar occultations by Saturn's rings observed with the Visual and Infrared Mapping Spectrometer (VIMS) onboard the Cassini spacecraft reveal that dusty features such as the F ring and the ringlets in the Encke and the Laplace Gaps have distinctive infrared transmission spectra. These spectra show a narrow optical depth minimum at wavelengths around 2.87 μm. This minimum is likely due to the Christiansen Effect, a reduction in the extinction of small particles when their (complex) refractive index is close to that of the surrounding medium. Simple Mie-scattering models demonstrate that the strength of this opacity dip is sensitive to the size distribution of particles between 1 and 100 μm across. Furthermore, the spatial resolution of the occultation data is sufficient to reveal variations in the transmission spectra within and among these rings. In both the Encke Gap ringlets and F ring, the opacity dip weakens with increasing local optical depth, which is consistent with the larger particles being concentrated near the cores of these rings. The Encke Gap ringlets also show systematically weaker opacity dips than the F ring and Laplace Gap ringlet, implying that the former has a smaller fraction of grains less than ~30 μm across. However, the strength of the opacity dip varies most dramatically within the F ring; certain compact regions of enhanced optical depth lack an opacity dip and therefore appear to have a greatly reduced fraction of grains in the few-micron size range. Such spectrally-identifiable structures probably represent a subset of the compact optically-thick clumps observed by other Cassini instruments. These variations in the ring's particle size distribution can provide new insights into the processes of grain aggregation, disruption and transport within dusty rings. For example, the unusual spectral properties of the F-ring clumps could perhaps be ascribed to small grains adhering onto the surface of larger particles in regions of anomalously low velocity dispersion.

1. Introduction

Stellar occultations observed by the Visual and Infrared Mapping Spectrometer (VIMS) onboard the Cassini Spacecraft have already provided constraints on the geometry of self-gravity wakes in the A and B rings (Hedman et al., 2007; Nicholson and Hedman, 2010) and the architecture of the Cassini Division (Hedman et al., 2010). However, these analyses only used a fraction of the information returned by VIMS, because they were based on light curves derived from a single spectral channel. During each occultation, VIMS simultaneously measures the opacity of the rings over a range of wavelengths from 0.85 to 5.0 μm, which includes the strong water–ice absorption band at 3.1 μm. Thus each stellar occultation can in principle provide high-spatial-resolution transmission spectra of the rings. In practice, the optical depth of most regions in Saturn's main rings does not vary with wavelength because nearly all of the particles in the main rings are much larger than the near-infrared wavelengths observed. In this geometrical optics limit the transmission is essentially independent of wavelength.

However, the transmission can vary with wavelength when the particles are comparable in size to the observing wavelength. Several features in Saturn's rings are strongly forward scattering in the visible and near-infrared, indicating that they are composed primarily of micron-sized grains (Horányi et al., 2009) and this has been confirmed for the F ring by detailed spectrophotometric

* Corresponding author.
E-mail address: mmhedman@astro.cornell.edu (M.M. Hedman).

0019-1035/$ - see front matter © 2011 Elsevier Inc. All rights reserved.
doi:10.1016/j.icarus.2011.02.025

analyses (Showalter et al., 1992; Vahidinia et al., 2011). Searches for transmission variations using Earth-based occultations of the F ring did not reveal any statistically significant trends at ultra-violet or visible wavelengths (Bosh et al., 2002), but VIMS occultations by the F ring and other similarly dusty ringlets in the A-ring's Encke Gap and the Cassini Division's Laplace Gap have revealed a narrow opacity dip in the transmission spectra near 2.87 μm. As discussed in detail below, this feature provides novel constraints on the composition and structure of these dusty rings. Of particular interest is the ability of near-infrared stellar occultations to discern variations in the rings' particle size distribution on finer spatial scales than otherwise possible.

Our analysis begins by describing the relevant observations and how they were processed to obtain light curves. Second, we examine an illustrative example of the transmission spectra and demonstrate how the observed feature can be explained in terms of the Christiansen Effect associated with the strong water–ice absorption band centered at 3.1 μm. We then discuss how the strength of this feature relates to the local particle size distribution. In the future, we expect that combining these transmission spectra with relevant reflectance spectra and phase curves will place tight constraints on the size distribution, but such a complete photometric analysis is beyond the scope of this paper. Instead, we turn our attention to the variations in the transmission spectra, which allow us to discern trends in the particle size distribution. We find that the strength of the opacity dip varies systematically among the different ringlets, demonstrating that these dusty rings do have somewhat different particle size distributions. In particular, we explore the spectral variations within the F ring itself, focusing on narrow regions where the spectral feature appears to be highly suppressed, indicating a reduced concentration of micron-sized particles. These features are likely a subset of the compact optical depth enhancements identified in both Cassini images (Murray et al., 2008; Beurle et al., 2010) and UVIS stellar occultations (Esposito et al., 2008; Meinke et al., 2010). Finally, we discuss possible interpretations of the observed spectral variations in terms of spatially-varying particle densities and velocity dispersions within these dusty rings.

2. Observations

VIMS is most often used to produce spatially-resolved reflectance spectra of planetary targets. However, VIMS is a flexible instrument that can also operate in an occultation mode (Brown et al., 2004). In this mode, the imaging capabilities are disabled, the short-wavelength VIS channel of the instrument is turned off and the IR channel obtains a series of spectra from a single pixel targeted at a star. The raw spectra are composed of 248 measurements of the stellar brightness between 0.85 and 5.0 μm with a typical resolution of 0.016 μm (in occultation mode, 8 channels are used to encode timing data). However, to save on data volume, these data are usually co-added prior to transmission to Earth, producing "summed" spectra consisting of 31 spectral measurements with a typical resolution of 0.13 μm. The raw data used in this analysis are the uncalibrated Data Numbers (DN) returned by the instrument. While these DN are linear measures of the photon flux (Brown et al., 2004), no attempt is made to convert these data to absolute fluxes here, although a mean instrumental thermal background spectrum has been subtracted from all the spectra for each occultation. A precise time stamp is appended to every spectrum to facilitate reconstruction of the occultation geometry.

Each occultation is geometrically navigated based on the positions of the star (obtained from the Hipparcos catalog, and adjusted to account for proper motion and parallax at Saturn) and the position of the spacecraft derived from the appropriate SPICE kernels. This information was used to predict the apparent position (radius and inertial longitude) of the star in Saturn's ring plane as a function of time in a planetocentric reference frame, taking into account stellar aberration. In nearly all cases, this estimate of the occultation geometry was confirmed to be accurate to within a few kilometers using the known radii of nearly circular gap edges in the outer A Ring from (French et al., 1993). The exceptions were the low-inclination stars *o* Ceti and *δ* Virginis, for which features could be tens of kilometers away from their nominal positions. In these cases, the fiducial position of Saturn's pole was adjusted slightly (by at most 0.015°) to bring these cuts into alignment with the other occultations. (Note that such corrections were not possible for the Rev 12 *o* Ceti occultation, which only covered the F ring.)

By the end of 2009, VIMS was able to detect the F ring, the three dusty ringlets in the Encke Gap and the so-called "Charming Ringlet" in the outer Cassini Division[1] in multiple occultations. The F ring has been observed clearly most often because of its greater optical depth, being detectable in all 87 occultation cuts where the star passed behind that ring. The Encke Gap ringlets and Charming Ringlet, by contrast, can only be clearly detected in cases where the signal-to-noise is sufficiently high and when the optical depth of the ringlet is sufficiently large because the star either happened to pass behind a clump in the Encke Gap ringlets or was observed at a very low ring opening angle. In this analysis, we will only consider occultations where the peak optical depth of these ringlets is at least five times the standard deviation of the apparent optical depth variations outside the rings. This includes 24 cuts through the Encke Gap ringlets and 16 cuts through the Charming Ringlet.

Tables 1–3 provide lists of all the relevant occultation cuts, along with the occultation times, spacecraft elevation angles and inertial longitudes of the observations and the Data Numbers of the raw stellar signal. These tables also indicate whether the spectra were returned from the spacecraft in a summed or unsummed (full-resolution) state, and provide various measures of the rings' opacity, which are derived using the following procedures: The data are first normalized so that the average signal levels are unity at each wavelength in empty regions adjacent to each ring feature. (138,000–139,000 km and 141,000–142,000 km from Saturn's center for the F ring, 133,510–133,540 km and 133,650–133,700 km for the Encke Gap ringlets and 119,980–120,020 km for the Charming Ringlet). The resulting transmission measurements T are then transformed into line-of-sight slant optical depths τ using the standard formula:

$$\tau = -\ln T. \quad (1)$$

Throughout this paper we will always use the symbol τ to designate observed *slant* optical depths, never *normal* optical depths. This is because the standard computed normal optical depths may not be valid for the numerous compact structures found in the F ring (Esposito et al., 2008; Murray et al., 2008; Beurle et al., 2010) and the Encke Gap ringlets. Only for the Charming Ringlet, which is relatively broad and shows little variation with longitude in images (Hedman et al., 2010), is the normal optical depth a sensible quantity. The tables therefore provide estimates of the maximum *normal* optical depth for the cuts through the Charming Ringlet, and the maximum *slant* optical depths through the F ring and the Encke Gap ringlets (the F ring tables also provide the minimum observed transmission T).

3. The Christiansen Effect in Saturn's dusty rings

The occultation data set that best illustrates the unique spectral characteristics of these dusty ringlets is the Rev 46 occultation of α

[1] This dusty ringlet is located at 119,940 km from Saturn center, within the Laplace gap in the outer part of the Cassini Division.

Table 1
Stellar occultations of the F ring.

Star	Rev	Ingress/ egress	Sum[a]	Date[b]	B^c (°)	Longitude[d] (°)	Max DN[e] 2.92 μm	Max DN[e] 3.19 μm	Min T[f] 2.92 μm	Min T[f] 3.19 μm	Max τ 2.92 μm	Max τ 3.19 μm	$\langle\rho\rangle$[g]
οCet	008	i	S	2005-144T05:00	3.45	20.12	994	1181	0.04	0.03	3.34	3.57	0.85
οCet	008	e	S	2005-144T08:04	3.45	−47.08	995	1178	0.03	0.02	3.43	3.92	0.80
οCet	009	i	S	2005-162T08:06	3.45	10.75	990	1164	0.01	0.00	4.95	5.34	0.81
οCet	009	e	S	2005-162T10:25	3.45	−37.57	998	1166	0.11	0.08	2.23	2.57	0.82
οCet	010	i	S	2005-180T12:39	3.45	3.58	1184	1370	0.00	0.00	5.43	5.39	0.83
οCet	010	e	S	2005-180T14:24	3.45	−30.30	1170	1355	0.01	0.01	4.30	4.49	0.84
οCet	012	i	S	2005-217T01:30	3.45	−13.27	1108	1294	0.07	0.05	2.66	3.10	0.80
οCet	012	e	S	2005-217T01:57	3.45	−13.27	1087	1274	0.03	0.02	3.59	3.74	0.85
αSco	013	i	S	2005-232T11:12	32.16	277.55	802	788	0.74	0.72	0.31	0.33	0.90
αSco	013	e	S	2005-232T14:17	32.16	8.79	753	741	0.19	0.19	1.65	1.67	0.90
αTau	028	i	U	2006-252T10:26	22.17	35.78	131	119	0.49	0.47	0.72	0.76	0.91
δVir	029	i	U, E	2006-268T22:29	2.38	209.86	124	124	0.36	0.32	1.03	1.15	0.92
δVir	029	e	U, E	2006-268T22:47	2.38	91.40	123	126	0.23	0.24	1.47	1.42	0.92
αSco	029	i	S	2006-269T06:35	32.16	201.05	717	735	0.23	0.23	1.46	1.49	0.89
RLeo	030	i	S	2006-285T01:59	9.55	335.59	62	96	0.40	0.39	0.90	0.94	0.89
RLeo	030	e	S	2006-285T02:51	9.55	260.51	60	94	0.34	0.35	1.09	1.04	0.89
CWLeo	031	i	U	2006-301T01:18	11.38	−14.16	210	384	0.28	0.27	1.26	1.32	0.88
αAur	034	i	S	2006-336T12:22	50.88	28.99	416	382	0.73	0.71	0.32	0.35	0.89
RHya	036	i	S	2007-001T16:27	29.40	200.10	332	407	0.21	0.18	1.57	1.71	0.88
αAur	041	i	S	2007-082T16:44	50.88	14.19	193	177	0.50	0.46	0.70	0.77	0.87
RHya	041	i	S	2007-088T06:01	29.40	−153.47	104	143	0.40	0.36	0.91	1.02	0.88
RHya	042	i	S	2007-105T16:28	29.40	276.03	113	155	0.57	0.56	0.56	0.59	0.78
αOri	046	i	U	2007-163T01:57	11.68	2.46	726	686	0.06	0.05	2.75	3.05	0.88
αSco	055	e	S	2008-003T11:23	32.16	52.44	747	781	0.18	0.16	1.71	1.84	0.88
RLeo	060	i	S	2008-063T15:06	9.55	87.88	454	563	0.00	0.00	5.62	5.36	0.84
RLeo	060	e	S	2008-063T16:46	9.55	135.87	447	554	0.01	0.01	4.24	4.48	0.88
RLeo	061	i	S	2008-074T06:57	9.55	89.78	421	532	0.04	0.03	3.23	3.56	0.87
RLeo	061	e	S	2008-074T08:30	9.55	133.90	416	527	0.46	0.42	0.77	0.88	0.85
αTrA	063	i	S	2008-092T02:37	74.19	275.28	234	238	0.82	0.82	0.20	0.20	0.93
αTrA	063	e	S	2008-092T07:12	74.19	322.90	236	236	0.42	0.42	0.87	0.87	0.96
RLeo	063	i	S	2008-094T12:33	9.55	77.21	367	480	0.07	0.06	2.72	2.83	0.86
RLeo	063	e	S	2008-094T14:35	9.55	144.71	362	471	0.29	0.26	1.23	1.36	0.87
RLeo	068	i	S	2008-140T15:33	9.55	68.79	41	53	0.49	0.35	0.72	1.05	0.79
RLeo	068	e	S	2008-140T18:10	9.55	150.91	56	74	0.45	0.46	0.80	0.78	–
CWLeo	070	i	S	2008-155T13:43	11.38	69.33	350	569	0.43	0.39	0.84	0.94	0.89
CWLeo	070	e	S	2008-155T16:53	11.38	149.47	371	566	0.25	0.21	1.40	1.56	0.87
γCru	071	i	S	2008-160T08:13	62.35	187.65	477	507	0.77	0.77	0.26	0.26	–
CWLeo	071	i	S	2008-162T17:13	11.38	70.65	174	365	0.20	0.19	1.59	1.67	0.94
γCru	072	i	S	2008-167T11:30	62.35	−172.71	641	673	0.78	0.76	0.25	0.27	0.86
γCru	073	i	S	2008-174T14:39	62.35	186.98	654	685	0.55	0.52	0.60	0.65	0.90
CWLeo	074	i	S	2008-184T00:16	11.38	73.85	140	230	0.16	0.13	1.82	2.04	0.87
CWLeo	074	e	S	2008-184T03:09	11.38	144.75	142	233	0.34	0.30	1.09	1.22	0.87
RLeo	075	i	S	2008-191T04:10	9.55	67.95	270	397	0.61	0.58	0.49	0.55	0.84
RLeo	075	e	S	2008-191T06:59	9.55	149.97	270	396	0.07	0.05	2.65	2.96	0.90
γCru	077	i	S	2008-202T18:16	62.35	186.19	139	153	0.28	0.28	1.26	1.26	0.95
RLeo	077	i	S	2008-205T06:22	9.55	70.60	288	418	0.11	0.10	2.23	2.31	0.87
RLeo	077	e	S	2008-205T09:03	9.55	147.28	289	418	0.35	0.31	1.04	1.17	0.85
γCru	078	i	S	2008-209T19:17	62.35	186.01	280	286	0.69	0.65	0.38	0.43	0.88
ηCar	078	e	S	2008-210T03:29	62.47	336.59	65	90	0.31	0.34	1.16	1.07	0.98
βGru	078	i	S	2008-210T09:15	43.38	−103.88	271	297	0.93	0.93	0.07	0.07	–
γCru	079	i	S	2008-216T11:55	62.35	185.09	697	726	0.84	0.81	0.18	0.21	0.88
RSCnc	080	i	S	2008-226T01:14	29.96	50.08	309	361	0.32	0.31	1.14	1.18	0.90
RSCnc	080	e	S	2008-226T08:18	29.96	161.65	295	346	0.44	0.41	0.82	0.90	0.90
γCru	081	i	S	2008-231T06:03	62.35	184.53	590	611	0.95	0.94	0.05	0.06	0.81
γCru	082	i	S	2008-238T14:39	62.35	184.24	719	742	0.83	0.81	0.19	0.21	0.88
RSCnc	085	i	S	2008-262T21:39	29.96	51.47	310	369	0.27	0.25	1.33	1.40	0.91
RSCnc	085	e	S	2008-263T04:37	29.96	159.88	309	367	0.66	0.63	0.42	0.46	0.94
γCru	086	i	S	2008-268T02:19	62.35	183.55	1030	1081	0.84	0.83	0.17	0.19	0.89
RLeo	086	i	S	2008-271T10:01	9.55	86.47	654	906	0.87	0.85	0.14	0.16	0.84
RLeo	086	e	S	2008-271T11:35	9.55	132.01	650	901	0.69	0.67	0.37	0.40	0.86
RSCnc	087	i	S	2008-277T15:26	29.96	52.12	326	383	0.17	0.12	1.78	2.14	0.84
RSCnc	087	e	S	2008-277T22:20	29.96	159.11	322	393	0.25	0.25	1.40	1.37	0.98
RLeo	087	i	U	2008-278T18:51	9.55	87.43	304	417	0.84	0.81	0.18	0.21	0.85
RLeo	087	e	U	2008-278T20:23	9.55	131.05	303	416	0.05	0.05	2.95	3.02	0.93
γCru	089	i	S	2008-290T03:30	62.35	183.34	704	733	0.77	0.75	0.27	0.29	0.89
RSCnc	092	i	S	2008-315T00:42	29.96	69.72	223	263	0.10	0.08	2.34	2.51	0.96
γCru	093	i	S	2008-320T15:30	62.35	−157.95	466	499	0.54	0.53	0.62	0.63	0.94
γCru	094	i	S	2008-328T00:26	62.35	192.12	269	283	0.09	0.10	2.37	2.25	0.89
ϵMus	094	i	S	2008-328T06:47	72.77	245.59	190	209	0.55	0.52	0.59	0.65	0.83
γCru	096	i	S	2008-343T10:54	62.35	−171.80	209	227	0.49	0.48	0.70	0.73	0.89
γCru	097	i	S	2008-351T10:12	62.35	188.11	856	925	0.37	0.34	1.00	1.08	0.88
γCru	100	i	S	2009-012T09:24	62.35	−149.72	390	403	0.79	0.77	0.24	0.26	0.86
αTrA	100	i	S	2009-013T02:58	74.19	237.01	25	19	0.16	0.40	1.81	0.91	–

(continued on next page)

Table 1 (*continued*)

Star	Rev	Ingress/ egress	Sum[a]	Date[b]	B^c (°)	Longitude[d] (°)	Max DN[e] 2.92 μm	Max DN[e] 3.19 μm	Min T[f] 2.92 μm	Min T[f] 3.19 μm	Max τ 2.92 μm	Max τ 3.19 μm	⟨ρ⟩[g]
αTrA	100	e	S	2009-013T10:44	74.19	334.80	20	11	0.35	0.12	1.04	2.13	–
γCru	101	i	S	2009-021T23:10	62.35	210.27	418	438	0.60	0.57	0.52	0.56	0.89
γCru	102	i	S	2009-031T12:23	62.35	−149.92	993	1047	0.79	0.76	0.24	0.27	0.87
TXCam	102	i	S	2009-034T23:01	61.29	341.45	49	69	0.61	0.63	0.50	0.46	1.01
γCru	104	i	S	2009-053T08:17	62.35	255.06	220	238	0.51	0.48	0.68	0.73	0.96
βPeg	104	i	S	2009-057T08:33	31.68	−3.47	293	309	0.91	0.89	0.10	0.12	0.85
γCru	106	i	S	2009-077T06:43	62.35	254.88	803	834	0.75	0.73	0.29	0.32	0.89
γCru	106	e	S	2009-077T12:47	62.35	306.80	757	815	0.38	0.38	0.96	0.96	0.93
RCas	106	i	S	2009-081T20:43	56.04	44.25	128	169	0.45	0.42	0.79	0.86	0.90
βPeg	108	i	S	2009-095T13:53	31.68	5.32	289	306	0.69	0.66	0.37	0.42	0.88
αAur	110	i	S	2009-129T10:35	50.88	−34.08	319	291	0.38	0.35	0.96	1.04	0.89
αAur	110	e	S	2009-129T17:59	50.88	−127.08	257	258	0.69	0.67	0.37	0.40	0.88
αSco	115	i	S	2009-208T22:14	32.16	173.78	2705	2866	0.12	0.10	2.11	2.31	0.90
αOri	117	i	S	2009-239T07:26	11.68	31.20	513	542	0.21	0.19	1.54	1.68	0.93

[a] Summation mode, *S* = spectrally summed, *U* = not spectrally summed, *E* = Spectrally edited.
[b] UTC time when star crossed 140,000 km in the ringplane.
[c] Elevation angle of star.
[d] Inertial longitude of the cut at 140,000 km in the ringplane.
[e] Maximum Data Number after summation.
[f] Minimum observed transmission through the ring. Data normalized to unity in the regions 138,000–139,000 km and 141,000–142,000 km.
[g] Weighted average of the ratio of optical depths at 2.9 and 3.2 μm in the region between 139,000 and 141,000 km. Only provided where the peak optical depth exceeds 10 times the standard deviation of the background.

Orionis by the F ring. Of the handful of occultations done at full-spectral resolution, this one has the largest stellar signal and the lowest minimum transmission (see Table 1). Furthermore, the observed part of the F ring was within Saturn's shadow, so there is no contamination from scattered ringshine. The one problem with this occultation is that the observed stellar signal was not completely stable, but instead drifted and oscillated by several percent even when there was no variation in the amount of ring material occulting the star (see Fig. 1), These variations probably occur because the star happened to fall near the edge of the instrument's instantaneous field of view, and thus the observed signal was especially sensitive to small jitters in the spacecraft pointing. Even so, this data set provides the highest signal-to-noise full-spectral-resolution measurements of the F ring's transmission spectra to date.

In order to obtain a profile of ring opacity versus wavelength from these data, we convert the F ring's optical depth profile at each wavelength into a single measure of opacity known as the normal equivalent depth (French et al., 1991):

$$\mathcal{D} = |\sin B_*| \int \tau dr, \tag{2}$$

where B_* is the ring opening angle to the star. This radially-integrated quantity has units of length, and the factor of $|\sin B_*|$ may be regarded as converting either the line-of-sight optical depth to normal optical depth for a flattened ring, or the radial integral into an integral in the sky plane for a spatially-diffuse ring. In principle, we could do the integral over the entire radial width of the F ring. However, in this case, we elected to integrate over only the most optically-thick strand in the occultation (i.e. between radii of 140,400 and 140,550 km, see Fig. 1) in order to maximize the signal-to-noise.

Fig. 2 shows the resulting plot of equivalent depth versus wavelength, along with the complex index of refraction for (crystalline) water ice derived by Mastrapa et al. (2009). Naively, one might expect a peak in the ring's opacity around the peak of the strong absorption band at 3.1 μm, but instead the most prominent feature in the data is a sharp dip in the opacity centered at 2.87 μm, just shortward of the 3.1 μm band. This rather counter-intuitive minimum in opacity (or maximum in transmission) is almost certainly due to the Christiansen Effect (Christiansen, 1884, 1885), an optical phenomenon that is observed in systems composed of many small particles like powders (Prost, 1968; Elachi and van Zyl, 2006) or ice clouds (Arnott et al., 1995; Liou et al., 1998). At most wavelengths, the opacity of such materials is due to a combination of absorption within, scattering from, and diffraction around the individual particles. However, near appropriately strong molecular absorption bands the particles' optical properties become strongly wavelength-dependent, and there can even be wavelengths where the particles' index of refraction has a real part n_r close to that of the background medium while the imaginary part n_i is still well less than unity. At these so-called Christiansen wavelengths, surface scattering and diffraction are strongly suppressed, and provided the particles are sufficiently small, this produces a dip in the overall opacity (Hapke, 1993; Elachi and van Zyl, 2006; Vahidinia et al., 2011).

Since the primary constituent of Saturn's rings is crystalline water ice (Cuzzi et al., 2009), and the ring particles are dispersed in free space, the F ring's Christiansen wavelengths should occur wherever crystalline water ice has both $n_r \simeq 1$ and $n_i \ll 1$. Examining the optical constants for crystalline water ice plotted in Fig. 2, we find the indices of refraction vary dramatically in the vicinity of the strong 3.1 μm absorption band, with n_r falling below unity between 2.87 and 3.10 μm. In this range of wavelengths, ice only has $n_r \simeq 1$ and $n_i \ll 1$ at 2.87 μm. Thus the deepest part of the observed opacity dip falls very close to the Christiansen wavelength for crystalline water ice,[2] providing strong evidence that the Christiansen Effect is indeed responsible for this feature.

The opacity dip at the Christiansen wavelength is only observed in the F ring and other similarly "dusty" ring features (see below). It is not seen in the icy main rings because the particles in these rings are all millimeters in size or larger (Cuzzi et al., 2009), and the Christiansen Effect is only important for wavelength-sized particles. This can be most easily understood by considering the extinction coefficient Q_{ext}, which is defined as the ratio of a particle's optical cross section (including loses due to both scattering and absorption) to its physical cross section. In general, the relationship between this parameter and the measured opacity of a ring is rather complex and depends on the width of the ring parti-

[2] Amorphous water ice at 80 K has a Christiansen wavelength at 2.84 μm, which is inconsistent with the observed feature (Vahidinia et al., 2011). This observation thus provides further evidence for the crystallinity of the ice in the rings (Cuzzi et al., 2009).

Table 2
Stellar occultations of the Encke Gap ringlets.

Star	Rev	Ingress/egress	Sum	Date	B (°)	Longitude of ring (°)	Longitude of Pan (°)	Max DN 2.92 µm	Max DN 3.19 µm	Inner ringlet			Central ringlet			Outer ringlet		
										Max τ 2.92 µm	Max τ 3.19 µm	$\langle\rho\rangle$[a]	Max τ 2.92 µm	Max τ 3.19 µm	$\langle\rho\rangle$[b]	Max τ 2.92 µm	Max τ 3.19 µm	$\langle\rho\rangle$[c]
oCet	008	i	S	2005-144T05:14	3.45	16.72	−106.73	999	1192	0.0344	0.0333	–	0.0344	0.0343	–	0.1154	0.1254	0.96
oCet	008	e	S	2005-144T07:50	3.45	−43.68	−38.83	1001	1188	0.1217	0.1199	0.98	0.0169	0.0171	–	0.0180	0.0196	1.08
oCet	009	i	S	2005-162T08:24	3.45	5.38	84.64	993	1164	–	–	–	0.0668	0.0697	0.98	–	–	–
oCet	009	e	S	2005-162T10:06	3.45	−32.19	128.65	1005	1181	0.0214	0.0249	–	0.0435	0.0416	–	0.0238	0.0254	–
oCet	010	i	S	2005-180T13:09	3.45	−6.38	−43.17	1176	1363	0.2788	0.2894	0.96	4.7709	5.2434	0.94	0.0527	0.0544	0.99
oCet	010	e	S	2005-180T13:55	3.45	−20.34	−23.14	1187	1376	0.0417	0.0403	0.95	0.1973	0.2091	0.94	0.0566	0.0551	1.00
δVir	029	i	U, E	2006-268T22:29	2.38	208.57	112.96	123	125	2.0838	1.9774	0.97	–	–	–	–	–	–
RHya	042	i	S	2007-105T17:24	29.40	279.35	78.51	113	157	–	–	–	–	–	–	0.2815	0.3127	0.95
RLeo	060	e	S	2008-063T16:32	9.55	130.43	−55.79	460	584	–	–	–	0.0241	0.0246	–	–	–	–
RLeo	061	i	S	2008-074T07:12	9.55	95.94	107.29	432	553	0.0626	0.0561	1.02	–	–	–	–	–	–
RLeo	061	e	S	2008-074T08:15	9.55	127.74	134.56	431	557	0.0361	0.0342	–	–	–	–	–	–	–
RLeo	063	i	S	2008-094T12:42	9.55	80.59	171.27	369	496	–	–	–	0.0259	0.0297	–	–	–	–
CWLeo	074	i	S	2008-184T00:28	11.38	77.01	34.87	146	248	–	–	–	0.5296	0.5531	1.00	–	–	–
CWLeo	074	e	S	2008-184T02:57	11.38	141.60	99.84	156	264	–	–	–	0.3642	0.3706	0.98	–	–	–
RLeo	077	i	S	2008-205T06:32	9.55	73.42	19.67	298	440	–	–	–	0.1009	0.1053	0.95	–	–	–
RLeo	077	e	S	2008-205T08:53	9.55	144.46	81.33	300	443	–	–	–	0.0401	0.0334	–	0.0612	0.0683	1.03
RSCnc	080	i	S	2008-226T01:28	29.96	51.58	74.51	311	363	–	–	–	–	–	–	0.2367	0.2459	0.93
RSCnc	085	e	S	2008-263T04:22	29.96	158.29	−86.66	314	377	0.0942	0.1015	1.00	–	–	–	–	–	–
RLeo	086	i	S	2008-271T10:15	9.55	92.33	34.91	668	932	–	–	–	0.0742	0.0730	0.98	0.0654	0.0668	0.97
RSCnc	087	e	S	2008-277T22:05	29.96	157.48	139.90	327	400	–	–	–	0.0325	0.0355	–	–	–	–
RLeo	087	e	U	2008-278T20:07	9.55	124.79	−5.27	315	439	0.0735	0.0643	–	–	–	–	–	–	–
γCru	104	e	S	2009-053T13:36	62.35	301.71	−104.92	167	184	–	–	–	0.1059	0.1130	–	–	–	–
βPeg	104	i	S	2009-057T08:42	31.68	−4.18	111.21	297	314	–	–	–	–	–	–	0.1348	0.1384	0.92
αOri	117	i	S	2009-239T07:32	11.68	31.82	−101.37	525	552	2.1787	2.2825	0.97	–	–	–	–	–	–

Data normalized to unity in the ranges 133,510–133,540 and 133,650–133,700 km.
[a] Weighted average of the ratio of optical depths at 2.9 and 3.2 µm in the range between 133,450 and 133,510 km. Only provided where the peak optical depth exceeds 10 times the standard deviation of the background.
[b] Weighted average of the ratio of optical depths at 2.9 and 3.2 µm in the range between 133,540 and 133,650 km. Only provided where the peak optical depth exceeds 10 times the standard deviation of the background.
[c] Weighted average of the ratio of optical depths at 2.9 and 3.2 µm in the range between 133,700 and 133,730 km. Only provided where the peak optical depth exceeds 10 times the standard deviation of the background.

Table 3
Stellar occultations of the Charming Ringlet.

Star	Rev	Ingress/ egress	Sum	Date	B (°)	Longitude (°)	Long. of Sun (°)	Max DN 2.92 μm	Max DN 3.19 μm	Max $\tau \sin B$[a] 2.92 μm	Max $\tau \sin B$[a] 3.19 μm	$\langle\rho\rangle$[b]
oCet	008	i	S	2005-144T05:53	3.45	2.37	172.68	1000	1185	0.0033	0.0038	0.83
oCet	008	e	S	2005-144T07:11	3.45	−29.33	172.68	1007	1196	0.0024	0.0026	0.83
αOri	026	i	S	2006-204T16:45	11.68	−2.26	−171.67	967	1013	0.0039	0.0047	0.87
αSco	029	i	S	2006-269T07:37	32.16	194.22	−169.40	713	729	0.0073	0.0091	–
RLeo	030	e	S	2006-285T02:40	9.55	274.44	−168.85	64	104	0.0279	0.0251	–
CWLeo	031	i	U	2006-301T01:26	11.38	−22.60	−168.29	164	319	0.0122	0.0090	–
αSco	055	e	S	2008-003T09:50	32.16	64.25	−153.79	728	761	0.0097	0.0108	–
RLeo	063	i	S	2008-094T13:08	9.55	94.78	−150.86	371	486	0.0063	0.0065	–
RLeo	063	e	S	2008-094T14:01	9.55	127.14	−150.86	372	491	0.0061	0.0068	–
RLeo	075	i	S	2008-191T04:41	9.55	79.61	−147.78	279	408	0.0067	0.0066	–
RLeo	075	e	S	2008-191T06:28	9.55	138.31	−147.78	280	411	0.0072	0.0075	–
RLeo	077	i	S	2008-205T06:56	9.55	83.90	−147.34	296	429	0.0053	0.0063	–
RLeo	077	e	S	2008-205T08:29	9.55	133.98	−147.34	297	433	0.0097	0.0073	–
γCru	097	i	S	2008-351T11:00	62.35	187.44	−142.76	808	869	0.0140	0.0161	–
αSco	115	i	S	2009-208T23:53	32.16	170.44	−135.88	2719	2877	0.0062	0.0064	–
αOri	117	i	S	2009-239T07:45	11.68	33.75	−134.95	547	572	0.0064	0.0064	–

[a] Normal optical depth, data normalized to unity between 119,980 and 120,020 km.
[b] Weighted average of the ratio of optical depths at 2.9 and 3.2 μm in the range between 119,880 and 119,980 km. Only provided where the peak optical depth exceeds 10 times the standard deviation of the background.

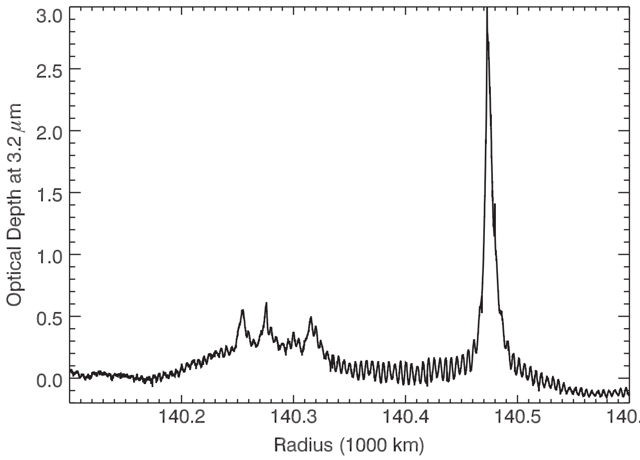

Fig. 1. Optical depth profile of the F ring at 3.18 μm as observed in the Rev 46 αOri occultation. The rapid periodic variations in optical depth are an instrumental artifact (see text). Nevertheless, this is the highest signal-to-noise occultation obtained at full-spectral resolution. We derive the transmission spectrum of the ring in Fig. 2 by integrating over the strong peak at 140,470 km.

cles' forward scattering lobe, as well as the apparent size of the observed ring feature and the instrument's field of view (Cuzzi, 1985; French and Nicholson, 2000). However, for rings composed primarily of sub-millimeter particles (which have broad forward-scattering diffraction lobes) the measured opacity is simply proportional to the appropriately weighted average of Q_{ext} over all the particles in the ring. For dielectric spheres Q_{ext} can be computed analytically (van de Hulst, 1957):

$$Q_{ext} = 2 - 4e^{-\chi \tan\beta}\left(\frac{\cos\beta}{\chi}\right)\left[\sin(\chi-\beta) + \frac{\cos\beta}{\chi}\cos(\chi-2\beta)\right] + 4\frac{\cos^2\beta}{\chi^2}\cos(2\beta). \quad (3)$$

Here $\tan\beta = n_i/(n_r - 1)$ and $\chi = (n_r - 1)4\pi s/\lambda$, n_r and n_i being the real and imaginary parts of the particle's refractive index, while s is the particle radius and λ is the wavelength of the incident light. For very small particles ($s \ll \lambda$), Q_{ext} approaches zero, while for large particles ($s \gg \lambda$), Q_{ext} asymptotes to 2 regardless of the assumed optical constants. However, at intermediate particle sizes where $x = 2\pi s/\lambda \sim 1$, Q_{ext} can vary dramatically depending on the assumed indices of refraction (see Fig. 3). Since the opacity of a diffuse cloud of particles is proportional to the appropriately weighted average of Q_{ext}, the precise values of the particles' optical constants will only be relevant to a ring's optical depth if there are sufficient particles of size $s \sim \lambda$. Thus the opacity of Saturn's main rings, where $s \gg \lambda$ for all particles, should be almost independent of wavelength, as observed, and only dusty rings should exhibit spectral features in their transmission spectra.

On a more detailed level, the magnitude of the opacity variations in the vicinity of the Christiansen wavelength can help constrain the particle size distributions in these dusty rings. Indeed, the curves in Fig. 3 provide insights into which aspects of the particle size distribution the opacity measurements probe. First consider the curve corresponding to $n = 1.33 + i * 0.0$, the typical index of refraction of water ice outside the strong absorption bands. In this case the primary sources of opacity are surface scattering and diffraction, and the periodic variations in Q_{ext} seen in this curve arise from interference among light rays taking different paths around or within the grains. These wiggles are very sensitive to the exact size and shape of the particles and are therefore likely to be washed out for any collection of realistically-shaped grains. However, even if ignore these ripples, there are still clear systematic differences between this curve and the two others, which are more representative of the optical constants near the strong 3.1 μm absorption band.

The $n = 1.00 + i * 0.1$ curve corresponds to water ice near the Christiansen wavelength of 2.87 μm (see Fig. 2). The extinction in this case is largely due to bulk absorption and is significantly lower than for the $n = 1.33 + i * 0.0$ case in the range $1 < x = 2\pi s/\lambda < 10$. Thus, ice-rich particles between 1 and 10 μm in diameter should have a *reduced* opacity at 2.87 μm compared to that at wavelengths far from the absorption band. We can therefore interpret the observed opacity dip in the F ring at 2.87 μm as evidence for a significant population of 1–10 μm-sized particles in this ring.

On the other hand, the $n = 1.00 + i * 0.5$ curve corresponds to the Q_{ext} of water ice around 3.1 μm, near the center of the absorption band. In this situation, the predicted Q_{ext} is noticably higher than the $n = 1.33 + i * 0.0$ case when $x = 2\pi s/\lambda < 2$. Thus particles smaller than 2 μm in diameter would tend to have a *higher* opacity at 3.1 μm than they do at other wavelengths. This would produce a peak in the opacity spectrum, which is *not* observed, and therefore suggests that sub-micron grains do not dominate the opacity of the F ring. This is consistent with the lack of a pronounced slope in the

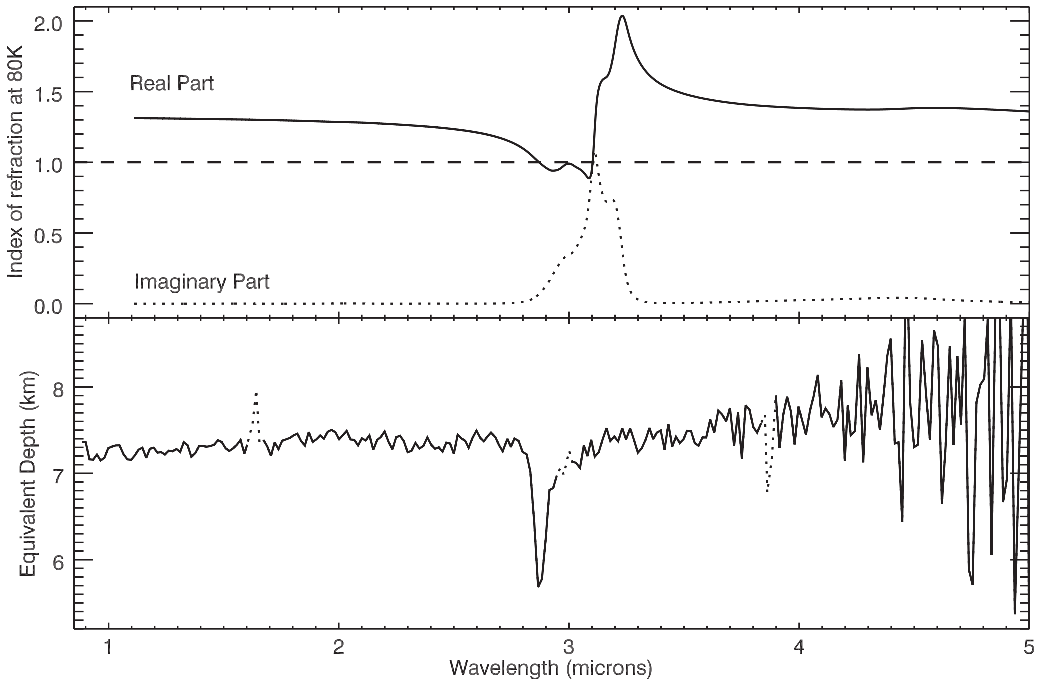

Fig. 2. Wavelength-dependent opacity of the F ring core, as observed in the Rev 46 αOri occultation. The top panel shows the real and imaginary components of the index of refraction of crystalline water ice at 80 K (Mastrapa et al., 2009), while the lower panel shows the equivalent depth of the core of the F ring as a function of wavelength. The dip in opacity at 2.87 μm occurs where the real part of the index of refraction first approaches unity. Dotted sections of the spectrum indicate boundaries between blocking filter segments, where the transmission estimates may be less reliable.

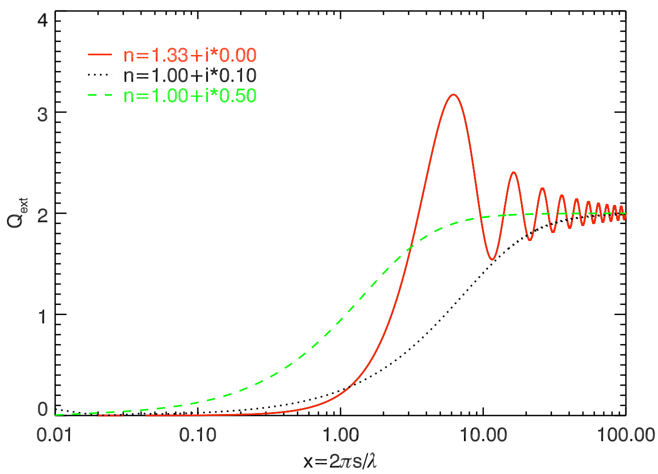

Fig. 3. Plot of the extinction coefficient Q_{ext} of spherical grains with different indices of refraction as a function of $x = 2\pi s/\lambda$. The $n = 1.33 + i * 0.0$ case corresponds to ice outside of strong molecular absorption bands, while the other two cases reflect the variations in the optical constants within the strong 3.1 μm absorption band.

transmission spectrum outside of the dip at 2.87 μm. If sub-micron grains were common in the ring, then far from the strong absorption band we would expect $Q_{ext} \propto (s/\lambda)^2$, which would produce a steep slope in the transmission spectrum which is not seen either here or in earlier ground-based occultation data (Bosh et al., 2002).

The above considerations suggest that only a rather limited set of particle size distributions will be able to reproduce the observed transmission spectrum. To test this supposition, we computed the predicted transmission spectra for various populations of particles using a Mie scattering code, assuming that all the particles are composed of pure crystalline water ice at 80 K. Initial investigations indicated that neither simple power laws nor narrow Hansen–Hovenier distributions could reproduce the observed transmission spectra. We therefore considered slightly more complex size distributions, and found that certain broken power laws could reproduce many of the salient features of the observed transmission spectra. In these models the particle size distribution follows a power law $n(s) \propto s^{-q_{small}}$ up to a critical size s_{break}, above which the size distribution changes to a different (steeper) power law $n(s) \propto s^{-q_{big}}$ (see Fig. 4). Fig. 5 shows the calculated extinction spectra for a range of models with different values of q_{big} and q_{small}, but the same value of s_{break} = 10 μm and an assumed maximum particle size of 1 mm. As expected, increasing q_{small}—which increases the fraction of micron-sized and smaller particles in the ring—causes the extinction spectrum to develop a prominent slope at short wavelengths and a peak at 3.1 μm. Since these features are not seen in the F-ring data, q_{small} needs to be rather low (around 2 assuming $s_{break} \sim 10$ μm). On the other hand, decreasing q_{big}—which increases the fraction of very large particles in the ring—tends to dilute the 2.87 μm opacity dip. Thus to produce an opacity dip of the appropriate magnitude q_{big} must be fairly high (around 3.5 assuming $s_{break} \sim 10$ μm). Together, these findings indicate that the size distribution must have a rather sharp break (with $q_{small} \sim 2$ and $q_{big} \sim 3.5$) to reproduce the observed transmission spectra. Such a break is consistent with other spectral data for the F ring (Vahidinia et al., 2011).

Of course, such transmission spectra alone cannot uniquely determine the particle size distributions of these rings. For example, different assumed values of s_{break} lead to somewhat different preferred values of q_{big}. Indeed, these data can only place limits on the fraction of the ring particles larger than 10 μm across, and do not strongly constrain the typical size of these larger particles. Furthermore, the ring particles are not spheres of pure water ice, and the detailed microstructure of the grains can alter the depth and location of the dip and complicate efforts to quantitatively constrain the particle size distribution (Vahidinia et al., 2011). Indeed, the observed dip occurs at slightly longer wavelengths than predicted by the simple models used here. Nevertheless, these

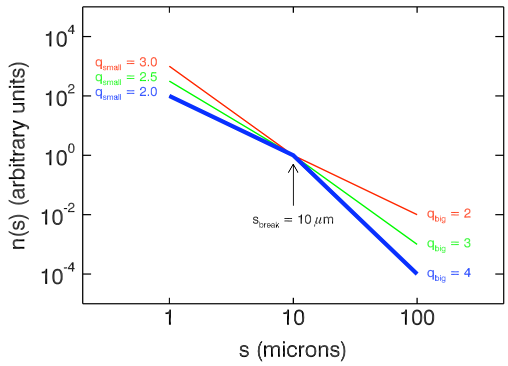

Fig. 4. Diagram illustrating the parameters used to describe broken power-law size distributions, which include two slopes q_{small} and q_{big}, as well as a break point s_{break}.

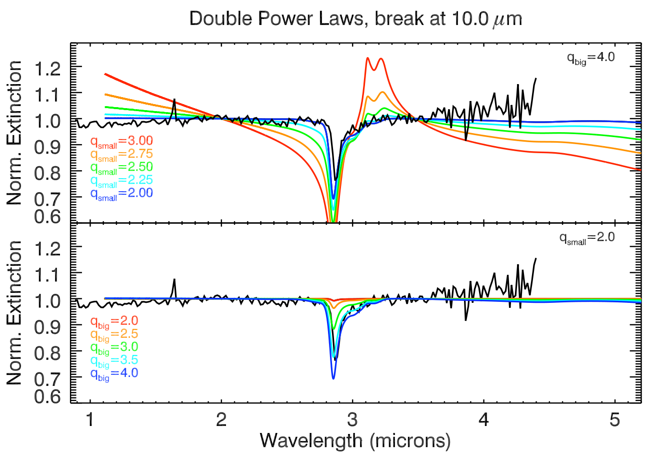

Fig. 5. Model extinction spectra for different particle size distributions compared with the observed spectra derived from the Rev 46 α Orionis occultation. All spectra have been scaled to unity at 2 μm in order to facilitate comparisons. All model spectra are for broken power laws with the break at a particle radius of 10 μm and a maximum particle size of 1 mm. All grains are assumed to be composed of pure crystalline water ice with optical constants given in Mastrapa et al. (2009). In the top panel, all the model distributions have a power-law index of 4 above the break, but a range of indices between 2 and 3 below the break. Note that as the number of small particles increases, the spectrum outside the 2.87-μm opacity dip develops prominent slopes that are not observed in the data. In the lower panel, all the model size distributions have indices of 2 below the break, but a range of indices above the break. In this case, we see that if there are too many large particles, then the opacity dip will become diluted and is too small compared to the observations.

transmission spectra still provide a unique resource for exploring *variations* in the particle size distributions of these dusty rings.

4. Comparisons among different dusty rings

The F ring and Encke Gap ringlets exhibit abundant structure and large variations in optical depth, so it is natural to ask whether their particle size distributions vary as well. By virtue of their high spatial resolution, the occultation data provide a unique avenue for investigating and quantifying any differences in the particle size distributions within or among these dusty rings. However, in practice we can only obtain a limited amount of spectral information from most of the occultations. In many occultations the total light observed by VIMS consists of a combination of both the desired starlight and sunlight reflected by the rings. This background ringshine is often sufficiently bright outside the strong 3.1 μm band that we cannot reliably measure any slope in the continuum transmission spectrum. On the other hand, the rings are always very dark at wavelengths near 3.1 μm, so the size and shape of the opacity dip are uncontaminated by ringshine. Unfortunately, most of the occultations were spectrally summed, so the spectral resolution of the measurements is insufficient to discern any changes in the width or shape of the opacity dip, leaving the magnitude of the dip as the only spectral feature that can be reliably determined for most of the occultations. Fortunately, even this single spectral parameter is sufficient to provide useful information about the variability of the particle size distribution in these dusty rings.

Fig. 6 illustrates how the opacity dip appears in the spectrally summed data. While the shape of the dip is no longer resolved, the spectral channel covering the range 2.87–2.98 μm (marked by a diamond) shows an equivalent depth that is clearly below its neighbors. By contrast, the spectral channel covering 3.13–3.25 μm (marked by a triangle) is clearly outside this dip. The main rings are observed to be quite dark at both these wavelengths due to absorption by water ice, so we can reliably quantify the magnitude of the opacity dip using the measured optical depths in these two summed spectral channels.

Given that the detailed microstructure of the dust grains can affect the depth and morphology of the opacity dip (Vahidinia et al., 2011), we will avoid any attempt to convert the absolute value of the opacity dip in the summed data into a constraint on the particle size distribution in the ring.[3] Instead, we will concentrate on trends in the depth of the opacity dip among and within the different rings.

For the rest of this analysis, we will quantify the magnitude of the opacity dip observed in the various dusty rings using the optical depth ratio:

$$\rho = \frac{\tau_{2.9}}{\tau_{3.2}}, \tag{4}$$

where $\tau_{2.9}$ and $\tau_{3.2}$ are the measured slant optical depths in the summed spectral channels covering the ranges 2.87–2.98 μm and 3.13–3.25 μm. These optical depths are computed from the appropriately normalized transmission profiles using the procedures described in Section 2 above, so for each occultation cut through the rings we can derive ρ as a function of radius.

While ρ itself is useful for studying variations in the opacity dip's strength within a single occultation cut, for comparing data from different cuts through different rings it is also worthwhile to have a radially-averaged optical depth ratio for each occultation cut through each ring feature. Simple radial averages are not appropriate in this situation because the value of ρ becomes ill-defined when the optical depth is low. Thus we instead compute a *weighted* average of ρ, where the weight is simply the optical depth at 3.2 μm:

$$\langle\rho\rangle = \frac{\int \tau_{3.2}\rho dr}{\int \tau_{3.2} dr} = \frac{\int \tau_{2.9} dr}{\int \tau_{3.2} dr} = \frac{\mathcal{D}_{2.9}}{\mathcal{D}_{3.2}}, \tag{5}$$

where $\mathcal{D}_{2.9}$ and $\mathcal{D}_{3.2}$ are the ring feature's equivalent depths at the two wavelengths (see Eq. (2)). Thus $\langle\rho\rangle$ is the ratio of the equivalent depths at 2.9 μm and 3.2 μm, which is the most sensible average statistic for a narrow ring.

The specific radial ranges used in the calculation of $\langle\rho\rangle$ differ for each ring feature. They are 139,000–141,000 km for the F ring, 133,450–133,510, 133,540–133,650 and 137,000–133,730 for the inner, central and outer Encke gap ringlets, and 119,880–119,980 km for the Charming Ringlet. The radial range for the F ring is deliberately broad in order to include all of its multiple strands and encompass its substantial orbital eccentricity (Bosh

[3] This caution is also justified because the last two spectral channels included in the summed 2.87–2.98 μm channel fall within a filter gap on the focal plane. While no evidence has been found that this gap allows light from other wavelengths to enter these channels, the absolute photometry could be compromised (see also Vahidinia et al., 2011).

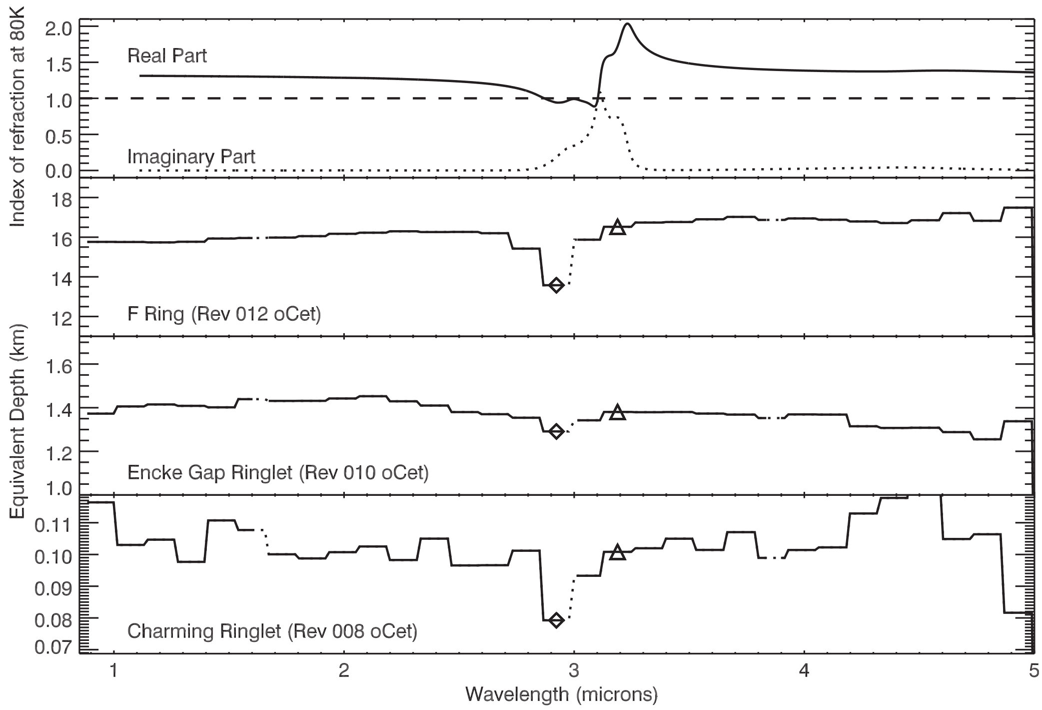

Fig. 6. The opacity of the F ring, an Encke Gap ringlet and the Charming Ringlet measured during occultations of the star *o* Ceti. The data here are all spectrally summed and therefore have lower resolution than the αOri data shown in Fig. 2. The diamond and the triangle mark the channels used to estimate the strength of the opacity dip (see text). All three spectra are of parts of the rings inside Saturn's shadow, and are computed by integrating over the radial ranges discussed in the text. Dotted lines in the spectra indicate filter gaps, as in Fig. 2. The indices of refraction are for crystalline water ice at 80 K (Mastrapa et al., 2009).

et al., 2002; Murray et al., 2008). When doing each integration we deliberately exclude all data where $\tau_{3.2}$ is less than 5 times σ_τ, the standard deviation of $\tau_{3.2}$ in the empty regions adjacent to the ring feature. We also exclude any data where the transmission falls below 0.1 (i.e. $\tau > 2.3$), in order to avoid regions where the optical depth may be saturated. The resulting values of $\langle\rho\rangle$ are recorded in Tables 1–3, but we will use both the localized, single-sample values of ρ and the radially-averaged quantities $\langle\rho\rangle$ in the discussions below.

Fig. 7 shows histograms of the derived $\langle\rho\rangle$ values for the various ring features. The shading in the histograms represent data with different signal-to-noise ratios, parametrized as the ratio of the peak optical depth at 3.2 μm (τ_{max}) to the standard deviation of the optical depth values (σ_τ) in nearby empty regions. Note that in both the Encke Gap and Charming Ringlet distributions, the data with τ_{max}/σ_τ between 5 and 10 are obviously more scattered than the data with τ_{max}/σ_τ greater than 10. This implies that the signal-to-noise is too low to obtain reliable $\langle\rho\rangle$ estimates when $\tau_{max}/\sigma_\tau < 10$. We therefore tabulate in Tables 1–3 the $\langle\rho\rangle$ values only for those observations where $\tau_{max}/\sigma_\tau > 10$.

Focusing exclusively on the higher significance data in Fig. 7, it is apparent that the different dusty rings have different distributions of $\langle\rho\rangle$. The F-ring distribution peaks around 0.9, but extends from below 0.8 to about 1.0. The three clear measurements of $\langle\rho\rangle$ from the Charming Ringlet all fall between 0.8 and 0.9, and therefore overlap the F-ring distribution. However, the Encke Gap ringlets seem to have $\langle\rho\rangle$ values between 0.95 and 1, which is clearly higher than typical values for the F ring.

Fig. 8 shows the $\langle\rho\rangle$ values versus the equivalent depth for the different rings (computed using Eq. (2) and the same radial ranges as employed in the calculations of $\langle\rho\rangle$). This plot demonstrates that the spectral differences between the Encke Gap ringlets and the F ring cannot be entirely ascribed to differences in these features' average optical depths. Even though the F ring's equivalent depth is almost always higher than the Encke Gap ringlets, there are cases

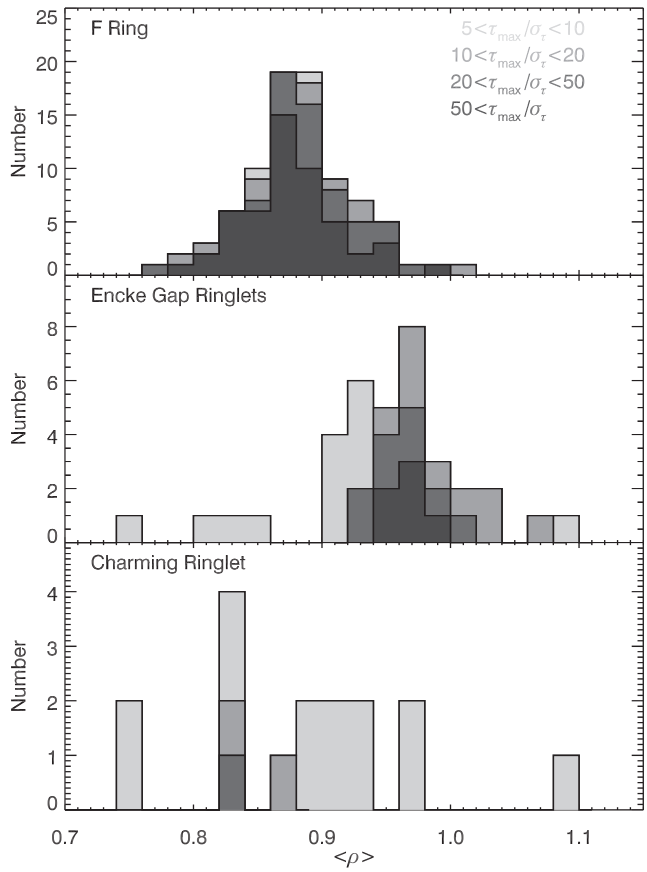

Fig. 7. Histograms showing the distribution of radially-averaged $\langle\rho\rangle$ values for the F ring, Encke gap Ringlets and the Charming Ringlet.The different gray levels correspond to values of the ratio τ_{max}/σ_τ as indicated, with lighter-toned histograms stacked on top of (not overlapping) the heavier-toned histograms.

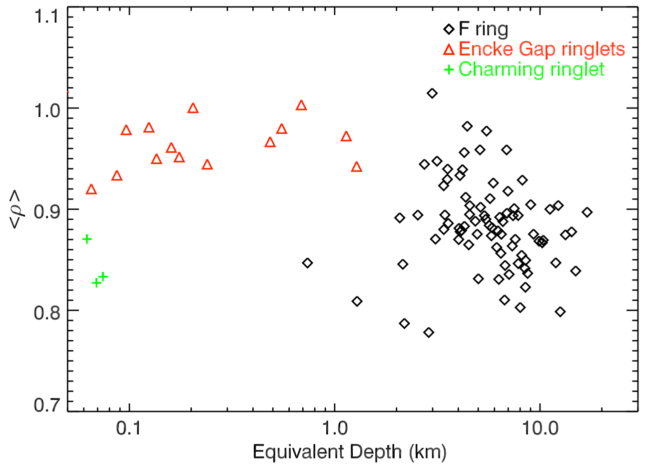

Fig. 8. Scatter plot showing the radially-averaged $\langle\rho\rangle$ values versus the equivalent depth of the ring at 3.2 μm. Only data with $\tau_{max}/\sigma_{\tau} > 10$ shown. The F ring data are the black diamonds, the Encke Gap ringlet data are the red triangles, and the Charming Ringlet data are the three green plusses.

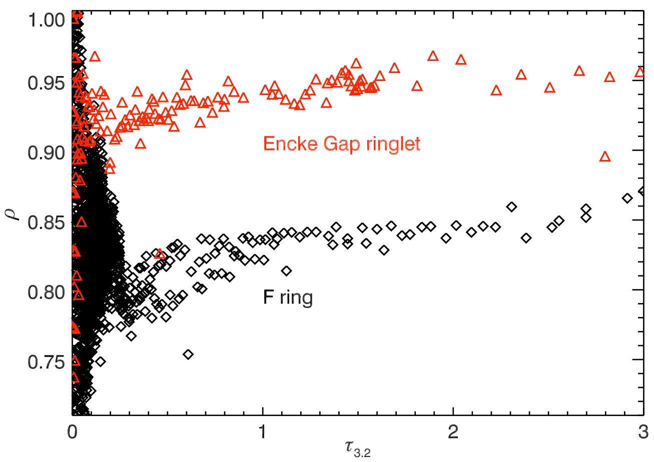

Fig. 9. Scatter plot showing the single-sample values of ρ versus slant optical depth for the F ring and central Encke Gap ringlet derived from the Rev 10 *o* Ceti ingress occultation, which happened to cut through a particularly dense clump in the Encke Gap ringlet. Note that at low optical depths, ρ becomes ill-defined leading to a large scatter in the measurements. While both features show a slightly increasing trend in ρ with optical depth, the Encke Gap ringlet has a consistently higher ρ than the F ring over a broad range of τ.

where the equivalent depth of these features are comparable to each other, and even in these situations the $\langle\rho\rangle$ values of the Encke Gap ringlets are systematically higher than those of the F ring. The Encke Gap ringlets and the F ring would therefore appear to have systematically different particle size distributions (see also Fig. 9). Since there is no evidence for a spike in the optical depth at 3.1 μm in any of the dusty rings (see Fig. 6), they all are probably depleted in sub-micron particles (cf. Fig. 5). However, the higher $\langle\rho\rangle$ values in the Encke Gap ringlets (corresponding to a weaker opacity dip at 2.87 μm) implies that these ringlets have a smaller fraction of particles in the 1–10 μm range. The size distribution of grains larger than 10 μm in the Encke Gap ringlets is therefore probably not as steep as it is for the typical F ring or the Charming Ringlet.

In addition to the systematic difference between the F ring and the Encke Gap ringlets, the finite widths of the $\langle\rho\rangle$ distributions in Fig. 7 also suggest that there are significant spectral and particle-size variations within each ring. Further evidence for such variations can be found in Figs. 9 and 10, which show single-sample estimates of ρ versus optical depth derived from occultations of the star *o* Ceti, which were obtained at a very low ring opening angle of 3.5° and hence provide exceptionally high signal-to-noise data for these rings. In both the Encke Gap ringlet and the F ring data there are clear trends of increasing ρ with increasing optical depth. The denser parts of these rings therefore have a smaller fraction of 1–10 μm particles, which would suggest that smaller grains are more widely dispersed in these rings than the larger ones. Note that in spite of these trends, Fig. 9 demonstrates that systematic differences between the Encke Gap and F ring persist even at the level of single-sample estimates of ρ.

However, while all the F-ring cuts show roughly similar rising trends, it is also clear that the detailed structure of the ρ–τ relationship differs from occultation to occultation (Fig. 10). The optical depth of the ring therefore cannot be the only factor controlling its spectral properties. This is consistent with the observation that occultation cuts of the F ring with similar equivalent depths can have a finite spread in $\langle\rho\rangle$ values (see Fig. 8, a similar spread is found if the $\langle\rho\rangle$ values are plotted versus maximum optical depth). This scatter in $\langle\rho\rangle$ is not obviously correlated with longitude relative to the F ring's pericenter or node, nor does it seem to be tied to the moon Prometheus (see Fig. 11). Thus this spectral variability seems to be independent of the broad-scale structure of the ring. Instead, the particle size distribution in the F ring is probably varying on the much smaller scales associated with the various clumps, strands, fans and other features that have been noted in Cassini images (Murray et al., 2008; Beurle et al., 2010).

5. Spectrally-distinct compact structures in the F ring

Interpreting the F ring's spectral variations is challenging because of the complex and time-variable nature of the F ring's morphology, which complicates efforts to correlate features observed at different times. However, there are certain features that are sufficiently compact and spectrally distinct to clearly stand out from the rest of the F ring. One of these features is illustrated in the top panel of Fig. 12, which shows the optical depth profile of the F ring obtained during egress of the Rev 013 α Scorpii occultation. This profile clearly shows two peaks, a broad one at 140,536 km and a narrow one at 140,546 km. Both of these peaks were also seen in the simultaneous UVIS occultation trace, which demonstrates that the narrow feature is a real ring structure and not an instrumental artifact (Esposito et al., 2008; Meinke et al., 2010). Comparing the optical depth profiles at 2.9 and 3.2 μm, we note that the broader peak is clearly less opaque at 2.9 μm than it is at 3.2 μm, consistent with the "typical" F ring, while the sharper peak has approximately the same opacity in both wavelength channels. This suggests that the narrow peak contains a much smaller fraction of micron-sized particles than the rest of the F ring.

Narrow optical-depth spikes like the one seen in this profile are particularly interesting because they represent the same sorts of compact objects that have been observed in both imaging (Murray et al., 2008; Beurle et al., 2010) and multiple UVIS stellar occultations (Esposito et al., 2008), and are attributed to either small moons or more transient clumps of debris. Studying these objects in detail has been difficult because they are embedded in a background of fine dust with complex, time-variable structure. This makes quantifying the size of these objects based on their brightness or opacity alone problematic, because the signal from the object itself cannot easily be distinguished from the signal from the surrounding dust. Some of these objects could even be nothing more than unusually dense clouds of dust, although others do appear to have sufficient mass to perturb nearby ring material (Beurle et al., 2010). The distinctive transmission spectra of these

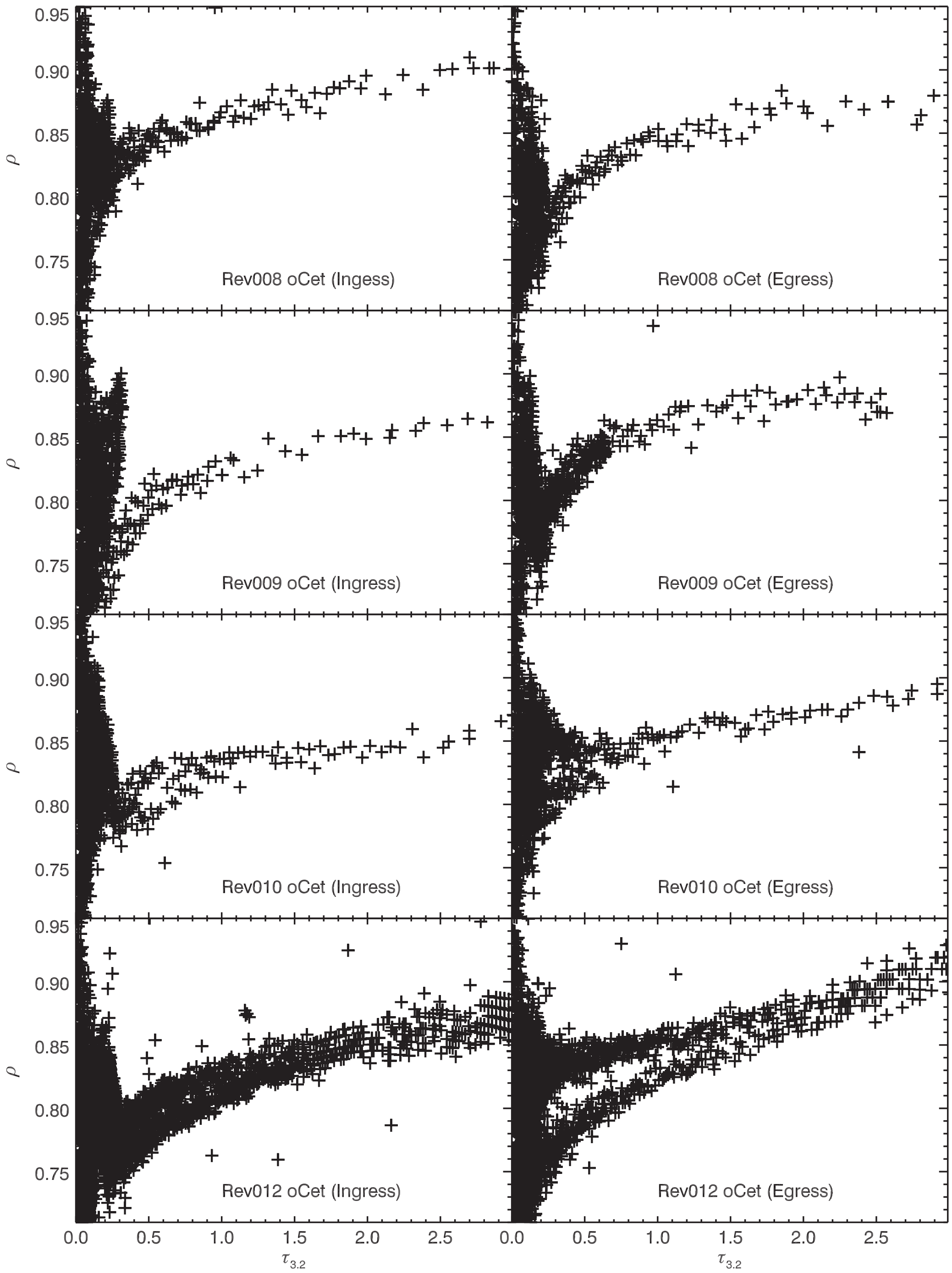

Fig. 10. Trends in the single-sample ρ values versus slant optical depth for the eight *o* Ceti occultations by the F ring. Note that at low optical depths, ρ becomes ill-defined leading to a large scatter in the measurements. All these profiles show the same basic trend of increasing ρ with increasing optical depth, consistent with the idea that larger particles are concentrated near the core of the ring. However, there are also significant variations in the shape of this trend among the different occultation profiles (The Rev 12 occultation track reached a minimum radius interior to the F ring, resulting in an exceptionally large number of samples within this ring).

objects in VIMS occultations may therefore provide useful new insights into these structures.

In order to better quantify the distinctive characteristics of the narrow peak in Fig. 12, consider the following two-component ansatz for the particle size distribution in the F ring: On the one hand, there is the "dust component" of the ring, consisting of particles smaller than ~30 μm, and on the other hand, there is a "big particle component" consisting exclusively of particles larger than ~30 μm. For this simple model, we will ignore the variations in the dust size distribution within the F ring discussed above and assume that the ratio of optical depths for the dust component is a constant $\rho_d = 0.9$ throughout the ring, where the specific value is chosen to be close to the peak of the distribution shown in Fig. 7. Similarly, we will assume the big particle component of the ring has an optical depth ratio $\rho_b = 1.0$. In this model, radial variations in the optical depth ratio ρ are interpreted as variations in the relative amounts of "dust" and "big particles" in different parts of the rings. More specifically, a sharp increase in ρ indicates an excess of particles larger than tens of microns across in that particular region of the ring. Let us denote the continuum (i.e., 3.2 μm) optical

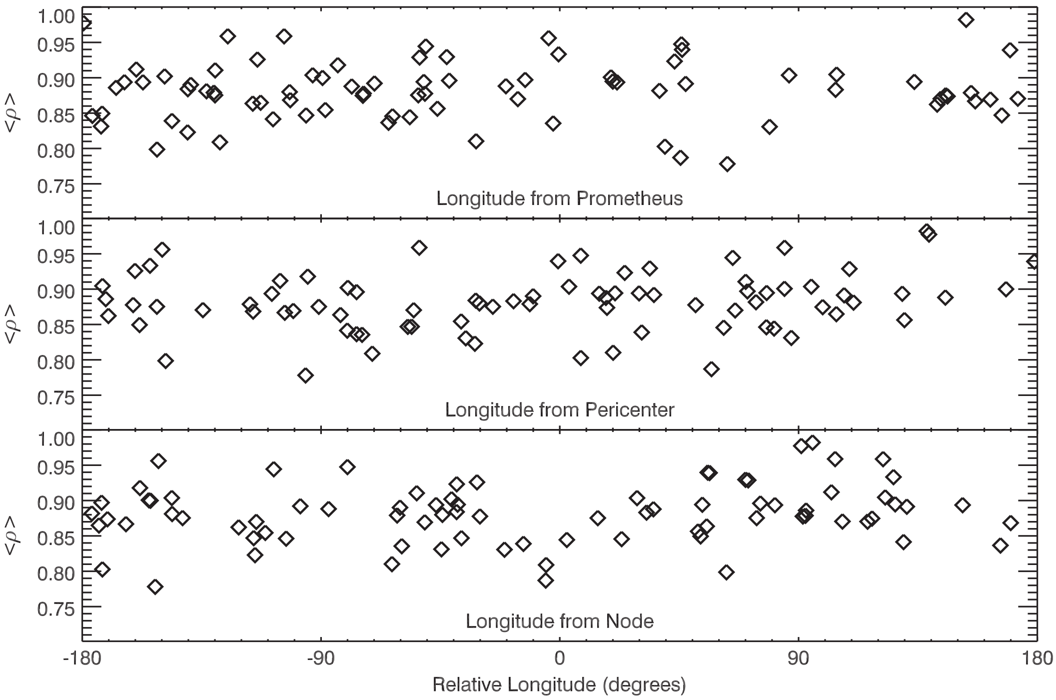

Fig. 11. Scatter plots of the radially-averaged $\langle\rho\rangle$ values for the F ring versus longitude relative to Prometheus and the F ring's pericenter and node (Model 12 of Albers et al. (in preparation)) No trend with any of these longitudes is evident in these data.

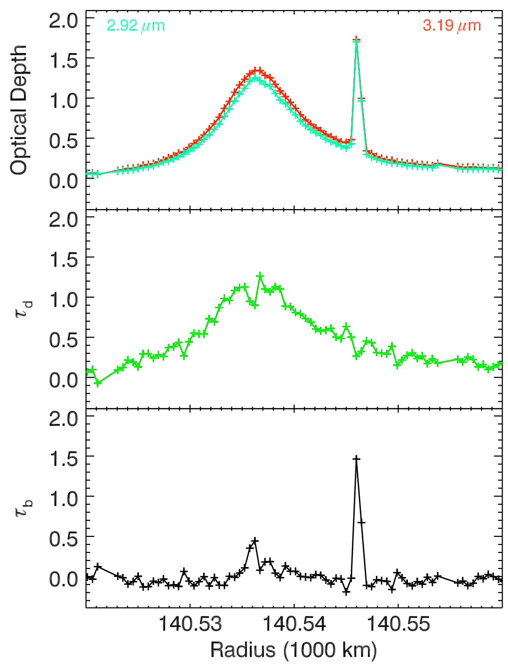

Fig. 12. Optical depth profiles from the Rev 013 egress α Scorpii occultation. The top panel shows the normal optical depth profiles at two wavelengths. Note that the broad peak shows a clear difference in its maximum opacity between the two curves, while the sharp peak at 140,546 km does not. The middle panel shows the inferred optical depth in dust, while the bottom panel shows the inferred optical depth in excess large particles (see text). The broad peak is prominent in the former, while the narrow spike is seen only in the latter, demonstrating that these two features have very different particle size distributions.

depths of these two components as τ_d and τ_b, respectively. Then the slant optical depths at our two standard wavelengths are given by:

$$\tau_{2.9} = \rho_d \tau_d + \tau_b, \tag{6}$$

and

$$\tau_{3.2} = \tau_d + \tau_b, \tag{7}$$

Solving these equations for τ_d and τ_b, we find:

$$\tau_d = \frac{1}{1-\rho_d}(\tau_{3.2} - \tau_{2.9}), \tag{8}$$

$$\tau_b = \frac{1}{1-\rho_d}(\tau_{2.9} - \rho_d \tau_{3.2}). \tag{9}$$

Fig. 12 shows profiles of τ_d and τ_b derived from the Rev 13 egress α Scorpii occultation using this method. Note that since $1 - \rho_d = 0.1$, the noise levels in these profiles are roughly 10 times larger than those of the individual spectral channels. Nevertheless, this decomposition clearly isolates the narrow spike from the rest of the F ring. Hence, even if the above model is a gross oversimplification of the real particle size distribution in the F ring, it provides a useful method of identifying these highly distinctive features, which appear to contain higher concentrations of large particles. It also confirms that at least this particular feature is significantly less dusty than other parts of the F ring.

Based on the above findings, we conducted a comprehensive search through the VIMS occultation data for other spectrally-identifiable compact structures. This search was done using an automated routine in order to minimize any subjective bias in feature identification. This algorithm is designed to find the most prominent spikes in τ_b profiles and uses multiple criteria to avoid flagging various artifacts. In particular, a cosmic ray strike in the 3.2 μm channel will cause a one-sample-wide spike in transmission and dip in opacity at that wavelength. This opacity drop reduces the apparent strength of the 2.87 μm dip and therefore produces a positive spike in the computed τ_b. Such artifacts can be distinguished from real features in the ring because the corresponding value of τ_d is strongly negative. Also, these features are always only a single sample wide. (Note that cosmic ray strikes in the 2.9-μm channel produce negative spikes in τ_b and therefore cannot be mistaken for a clump.)

Table 4
Features with distinctive transmission spectra in the F ring.

Star	Rev	Ingress/ egress	SCET (s)	Subspacecraft longitude	Subspacecraft latitude	Radius (km)	Longitude (°)	S	Peak τ_b	τ_d[a]	Predicted radius (km)	Prometheus radius (km)	Prometheus long. (km)
αSco	013	e	1503240353.106	−26.9	32.2	140546.2	9.99	6.5	1.47	0.07	140530.7	139067.8	−94.27
αSco	029	i	1537945646.520	−82.1	32.2	139916.0	−158.36	7.7	1.24	0.47	139906.8	139250.6	5.88
αSco	055	e	1578052761.191	−44.5	32.2	140008.4	51.46	5.7	0.86	0.97	140013.2	139132.0	102.30
γCru	073	i	1592839004.290	−144.2	62.3	140182.9	−172.91	3.3	0.24	0.31	140193.6	139347.2	167.64
γCru	077	i	1595271275.846	−144.6	62.3	139906.5	−173.71	3.1	1.50	−0.41	139901.6	139686.0	140.67
RSCnc	087	e	1601766034.355	−174.4	−30.0	140478.2	159.87	4.6	1.61	−0.03	140492.0	139685.2	7.00
γCru	093	i	1605456599.050	−137.4	62.3	140078.4	−158.08	6.6	0.66	0.06	140090.0	139147.5	−107.59
γCru	094	i	1606093583.558	−140.0	62.3	139947.7	−167.88	3.1	2.53[b]	0.07	139959.8	139188.8	−97.80
γCru	097	i	1608115920.990	−141.6	62.3	139954.1	−171.83	3.6	0.33	0.65	139945.0	139182.2	−31.62
γCru	104	i	1613984114.746	−124.3	62.3	140511.1	−107.02	3.9	0.58	0.06	140510.8	139174.6	−103.71
γCru	106	e	1616074308.867	−114.5	62.3	140523.3	−51.12	3.4	0.18	0.13	140531.9	139648.6	63.74
γCru	106	e	1616074311.376	−114.5	62.3	140530.2	−51.12	10.9	1.06	0.25	140531.9	139648.6	63.73
αSco	115	i	1627426537.697	−70.3	32.2	140078.1	174.10	13.5	0.74	0.66	140110.9	139370.7	−172.84
αSco	115	i	1627426568.854	−70.2	32.2	139972.3	174.09	5.1	0.11	0.09	140110.8	139369.6	−172.63

[a] Note a low-pass filter is applied to the τ_d profile prior to calculating these estimates, so the values in this table are somewhat different from those shown in Figs. 13,14.
[b] The peak calculated τ_b is 4.33, but the peak $\tau_{3.2}$ is 2.53, and this a more reliable estimate of the optical depth of this feature.

To identify statistically significant features in the F ring, we first need to quantify the uncertainties in the parameters τ_b and τ_d for each profile. This is done by removing a smoothed version of the relevant profiles (smoothing length 100 km) and computing the *rms* variations of the filtered values of τ_b and τ_d in regions outside the rings (138,000–139,000 km and 141,000–142,000 km). These *rms* variations are denoted σ_b^o and σ_d^o and characterize the uncertainty in these parameters when the transmission is close to unity. Since the measurement uncertainties are linear in transmission and not in optical depth, the uncertainty in τ_b and τ_d when the opacity is finite depends on the background optical depth. Fortunately, the DN levels for the VIMS occultations are sufficiently high that the effects of Poisson counting statistics can be neglected, and using standard error propagation we can estimate the *rms* noise levels in τ_b and τ_d as:

$$\sigma_{b,d} = \sigma_{b,d}^o / T_{3.2} \tag{10}$$

where $T_{3.2}$ is the observed transmission of the rings at 3.2 μm.

A real spectrally-distinct region in the ring will have a significantly positive value of τ_b, and should not have a significantly negative value for τ_d. Also, the region will only be spectrally identifiable if the transmission is not so low that any spectral feature would be saturated. Finally, features only one sample wide are more likely to be instrumental or noise artifacts than features with a finite width. Based on these considerations, we developed the following four criteria to identify whether a given measurement of τ_b and τ_d in an occultation represents part of a spectrally distinctive feature in the ring:

- The ratio τ_b/σ_b of that sample must be greater than a threshold value S.
- The average ratio τ_b/σ_b of that sample and its two nearest neighbors must be greater than $S/\sqrt{3}$.
- The ratio τ_d/σ_d of that sample must be greater than -1.
- The transmission in that sample must be greater than 0.1 (i.e. the optical depth $\tau_{3.2}$ must be less than 2.3).

The first criterion selects the most significant features in the τ_b profiles, while the second and third are used to reject noise spikes and cosmic rays. The last criterion ensures that we have sufficient signal-to-noise to discern spectral variations. Note that this cut explicitly removes the most opaque features in the ring, so this search algorithm will not be able to identify spectrally-distinct features in the core of the F ring in the roughly dozen occultations where the peak optical depth exceeds 2.3. However, as we will see below this algorithm was able to identify one feature with a peak optical depth of over 2.5 because samples adjacent to the saturated one showed the required spectral signature. Beyond the second criterion's requirement that adjacent samples must show evidence of a coherent structure, these criteria make no *a priori* assumption about the radial extent of these features.

Table 4 lists the 14 features identified with this technique using a threshold value $S = 3$. Relaxing this threshold significance reveals additional features that may in fact be clumps, but also admits some structures that visually appear to be no more than statistical noise in regions where the total optical depth is high. Thus for the purposes of this analysis we will focus exclusively on these 14 highest signal-to-noise features.

Figs. 13 and 14 illustrate the radial profiles of these features. In each case, the τ_b profile shows a relatively compact structure less than 10 km wide, while the τ_d profile is fairly smooth (even in cases like the Rev 106 γ Crucis occultation where the optical depth profile contains multiple peaks), which confirms that spectral decomposition works sensibly in all of these cases, despite the variations in the background ρ of the dust. While many features

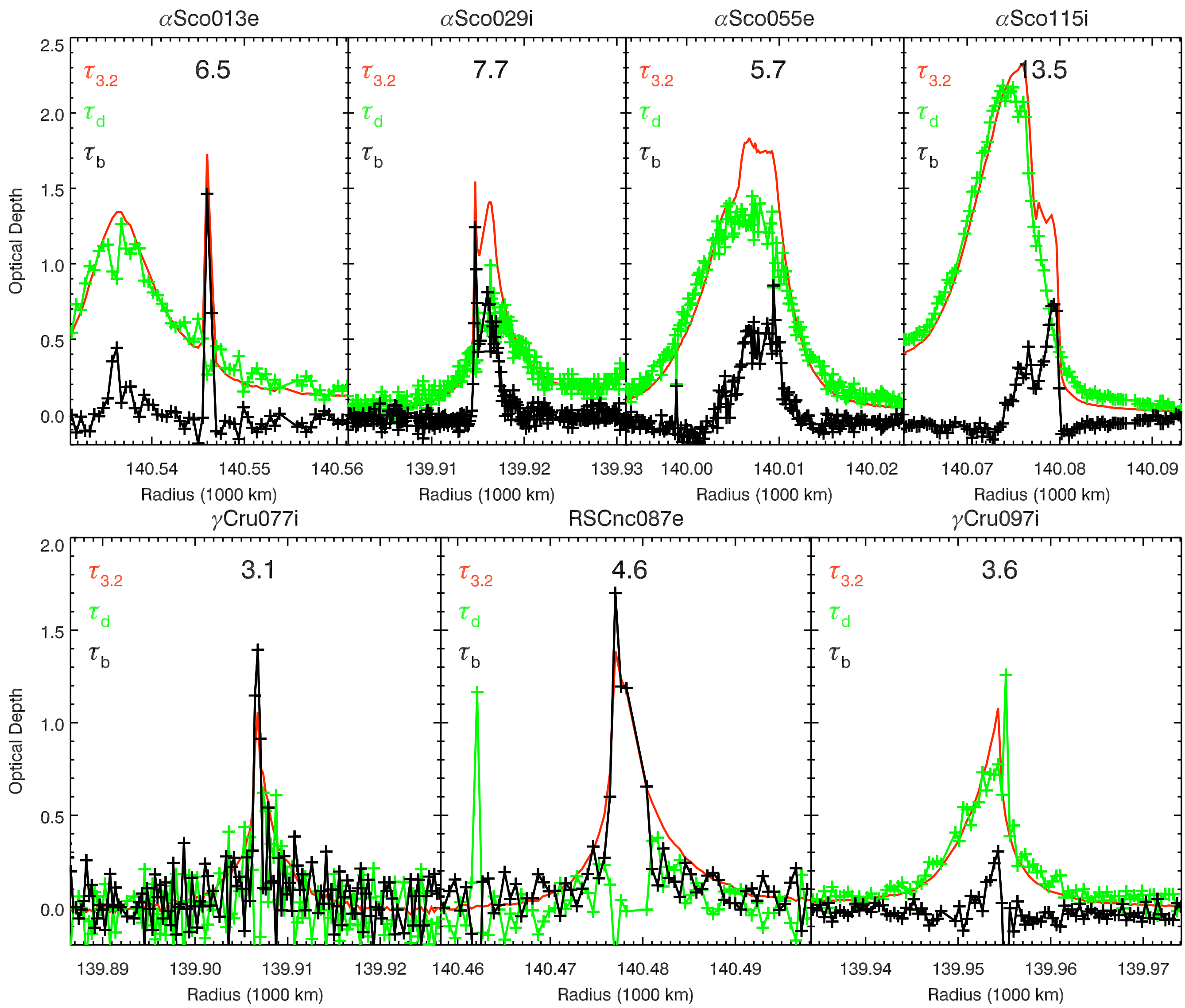

Fig. 13. Profiles of the $S > 3$ spectrally-distinct clumps identified by our automated search. In each plot, the smooth red curve is the measured optical depth, and the black and green curves are τ_b and τ_d, respectively. The numbers on the plot give the peak S value for each feature. The γCru 77 ingress data have been down-sampled by a factor of two for clarity. Note the αSco 115 feature is one of two clumps seen in this occultation, the other of which is found in a peripheral F-ring strand and is shown in Fig. 14.

correspond to obvious spikes in the optical depth profiles and therefore could have been identified based on their morphology alone (cf. Esposito et al., 2008), several of these features appear as rather subtle features in the optical depth profile and would be difficult to identify if not for their unusual spectral properties.

None of these features is opaque (the highest observed optical depth associated with these features being 2.5), so none of these features can be ascribed to a resolved moonlet in the F ring similar to that found in the α Leonis UVIS occultation (Esposito et al., 2008). Instead, what we appear to be seeing are relatively compact clumps of debris with enhanced large particle populations.

The morphologies of these debris clouds are quite diverse, and include:

- Isolated sub-kilometer-wide spikes (αSco013, γCru073, γCru094, and αSco115 at 139,972 km).
- Clusters of multiple narrow spikes (γCru093).
- Broader features several kilometers wide (αSco055, RSCnc087, and αSco115 at 140,078 km).
- Combinations of sub-kilometer spikes with more diffuse features (αSco029 and γCru106).

The latter two types of features only become obvious through the spectral decomposition, and reveal that these clumps can have significant substructure. Note the signal-to-noise of the γCru077, 097 and 104 occultations are low, so the morphologies of these three features are difficult to determine.

Some have argued that these clumps in the F ring arise from accretion of material initiated by the orbital perturbations produced by close encounters with Prometheus (Beurle et al., 2010), and there have even been attempts to demonstrate this connection with Prometheus by looking for clustering of these features in longitude relative to Prometheus (Meinke et al., 2010). Fig. 15 shows the distribution of the high-quality spectrally-identifiable features in longitude relative to Prometheus. We find no evidence for clustering in these data. This figure also shows the distribution of these features in longitude relative to the F ring's pericenter and node. Here there may be some hints of clustering, but the evidence is weak. These data do not provide convincing support for the idea that these particular clumps are organized in any coherent way on large spatial scales in the F ring. However, the absence of this particular observational signature does not rule out the possibility that Prometheus is responsible for at least some of these F ring

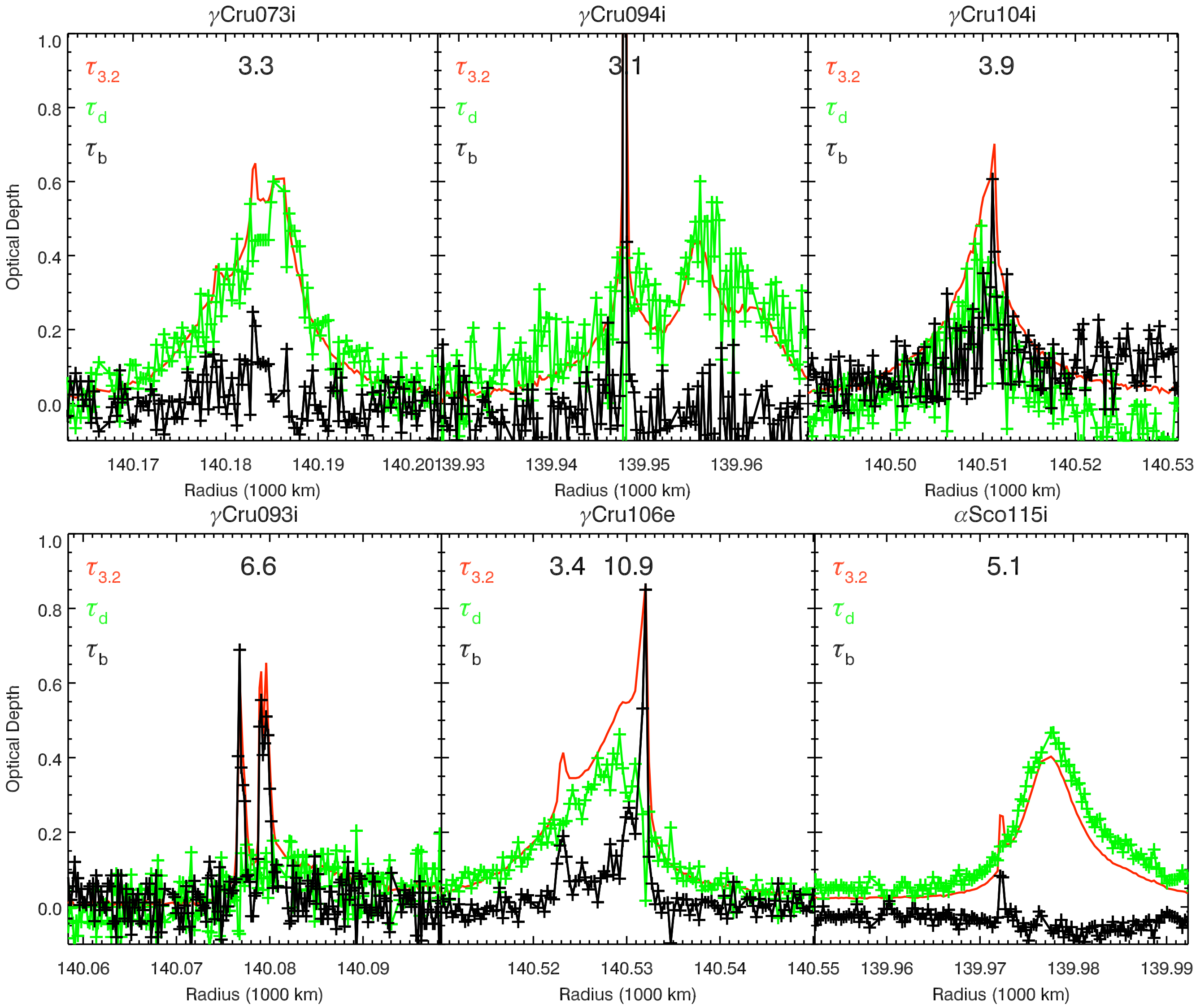

Fig. 14. Profiles of the $S > 3$ spectrally-distinct clumps identified by our automated search. In each plot, the smooth red curve is the measured optical depth, and the black and green curves are τ_b and τ_d, respectively. The numbers on the plot give the peak S value for each feature. The γCru 094, 104 and 106 data have been down-sampled by a factor of two for clarity. Note the αSco 115 feature is one of two clumps seen in this occultation, the other of which is found in the core of the F ring and is shown in Fig. 13.

features. Perturbations in the F ring induced by Prometheus close encounters can sometimes persist for more than one synodic period (Murray et al., 2008; Beurle et al., 2010), and if these knots correspond to the locations of these spectrally-identifiable features, we might expect their distribution to be roughly uniform in longitude.

6. Discussion

The variations in the transmission spectra described above can be divided into two types: those that appear to be correlated with optical depth (such as the trends seen in Figs. 9 and 10) and those that are not (such as the systematic spectral differences between the Encke Gap ringlets and the F ring in Fig. 8, or between the spectrally-distinctive clumps and the rest of the F ring in Fig. 12). While all of these spectral variations must reflect differences in the local particle size distribution, the physical processes responsible for the trends with optical depth are likely very different from those that distinguish the Encke Gap ringlets and F-ring clumps from the typical F ring and Charming Ringlet. Thus we will consider these two phenomena separately below.

6.1. Spectral variations correlated with the rings' optical depth

In both the F ring and the Encke Gap ringlets, the dip in the extinction spectra tends to be stronger in regions of lower optical depth (see Figs. 9 and 10), so the fraction of particles in the 1–10 μm size range increases as the optical depth decreases. Larger ring particles therefore appear to be more concentrated in the denser parts of the rings, while the smaller particles seem to be more widely dispersed in space. There are multiple physical processes that could potentially lead to this particle stratification. For example, any non-gravitational forces that might be perturbing these particles' orbits would tend to produce larger accelerations with smaller grains, dispersing them over a wider area of phase space. Alternatively, under certain conditions particle–particle interactions such as physical collisions or even Coulomb scattering could affect the orbital elements of small particles more than larger particles, and thus produce a more dispersed population of small grains. Detailed investigations of these phenomena (which are beyond the scope of this work) should therefore lead to a better understanding of these rings' local environment and the particles' charge states and surface properties.

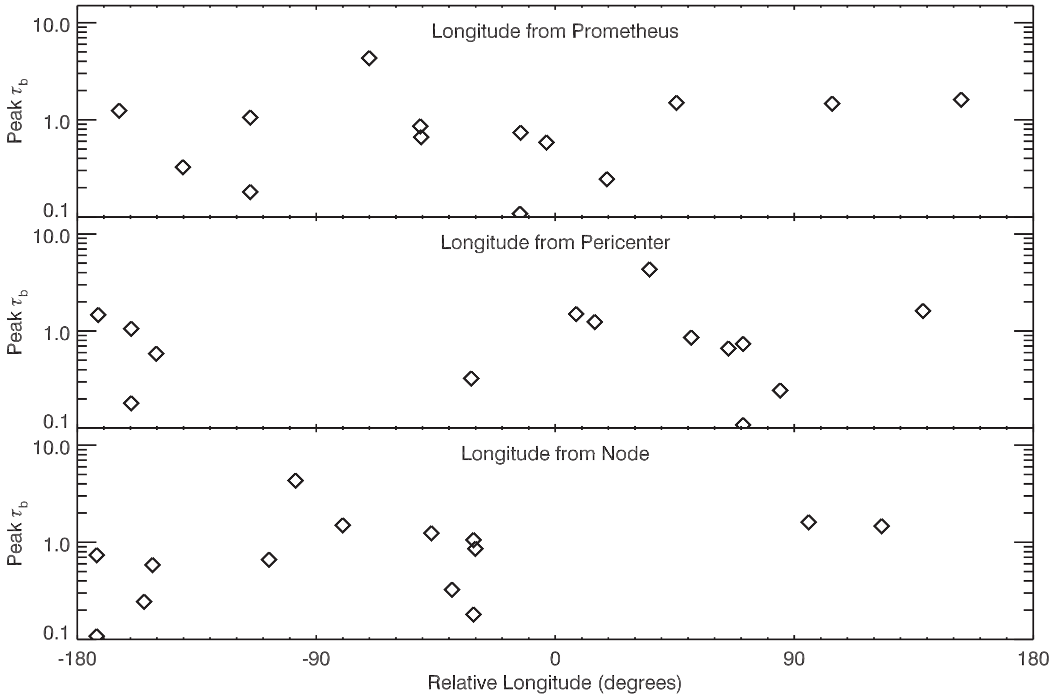

Fig. 15. The distribution of spectrally-identifiable regions in the F ring listed in Table 4 in optical depth and longitude relative to Prometheus and the F ring's pericenter and node.

6.2. Spectral variations not correlated with the rings' optical depth

The two most striking spectral variations that are not correlated with the rings' optical depth are (1) the systematically weaker opacity dips in the Encke Gap ringlets compared to the Charming Ringlet and typical F ring (cf. Figs. 8 and 9), and (2) the strongly attenuated opacity dips in certain compact regions within the F ring (cf. Fig. 12). These spectral features indicate that the Encke Gap ringlets and certain compact features in the F ring have smaller fractions of few-micron-sized particles than regions of comparable optical depth in the typical F ring and Charming Ringlet. Such differences in the local particle size distribution are likely due to some change in the balance between dust production, accretion, fragmentation and loss. Given that multiple aspects of these rings' dynamical environment influence these processes, a complete investigation of these features is well beyond the scope of this report. Instead, we will briefly consider one particular phenomenon that may be relevant: variations in the rings' local velocity dispersion altering the outcome of collisions among ring particles.

Despite the low overall optical depth of these rings, collisions among particles within the ring are not extremely rare. The relevant collision rate is proportional to the product of the particles' orbital mean motion and the ring's local optical depth. While the typical optical depths of these rings are rather low (<0.1), the orbital frequencies are sufficiently high (>1/day) that the timescale for collisions is rather short, being only weeks or less in the typical F ring. These collisions can have a significant impact on the ring's particle size distribution because, depending on how fast particles of different sizes approach each other, they can either stick together, bounce apart or fragment into pieces.

Güttler et al. (2010) provide detailed maps of collision outcomes versus particle size and impact speeds for non-icy particles, which show that the transitions between sticking and bouncing for silica-rich dust grains and aggregates are size-dependent and typically fall in the range between 0.01 and 100 cm/s. While the precise locations of these transitions will likely be different for the ice-rich ring particles, elementary theoretical calculations indicate that the relevant threshold speeds are of a similar order of magnitude. In particular, the threshold speed separating bouncing from simple sticking (without compaction) should occur when the impact energy equals $5E_{roll}$, where E_{roll} is the energy dissipated when two particles roll over each other by 90°, which depends on the material content and size of the grains (Dominik and Tielens, 1997; Güttler et al., 2010). The corresponding impact speed for identically-sized grains of mass m and radius R can be written as:

$$v_{crit} = \sqrt{\frac{5E_{roll}}{m}} = \sqrt{\frac{45\pi\gamma\xi_{crit}}{4dR^2}} \tag{11}$$

where d is the mass density of the particles, γ is the interface energy and ξ_{crit} is a critical rolling displacement. For ice, these numbers have been approximated as $d = 1\ \mathrm{g/cm^3}$, $\gamma \sim 100\ \mathrm{erg/cm^2}$ and $\xi_{crit} \sim 8$ Å (Wada et al., 2009). Inserting these values in the above expression, we find $v_{crit} \sim 20$ cm/s (10 μm/R). Thus particles smaller than 10 μm across could begin sticking to other particles whenever the collision velocities fall below 20 cm/s. Of course, other processes such as the compaction of loose aggregates could potentially complicate the situation, but even so v_{crit} should still provide a useful fiducial impact speed below which particles are more apt to stick together. Thus, any dynamical process that reduces the local velocity dispersion within these rings much below ~20 cm/s could lead to a depletion of small grains.

Recent simulations of the interactions between Prometheus and the F ring have demonstrated that the moon's perturbations on the ring particle's orbits can produce localized regions of enhanced density and reduced velocity dispersions (Beurle et al., 2010). The lowest velocity dispersions observed in these simulations are of order 2 cm/s, well below the critical speed for simple sticking with 10 μm grains. The spectrally-distinct compact regions in the F ring could therefore be interpreted as regions where interactions with Prometheus have increased the local particle density and decreased the local velocity dispersion, making it more likely that the 1–10 μm grains would have become attached to larger grains. The lack of correlation between the compact regions and longitude relative to Prometheus is not a major problem for this model if the disturbed regions persist for multiple synodic cycles and thus are roughly equally likely to be found anywhere around the ring. This interpretation would also be consistent with the emerging idea that some compact structures in the F ring could represent the accretion of material within the rings (Beurle et al., 2010; Meinke et al., 2010). In this case, the VIMS data would provide the first direct evidence for small grains adhering together to form larger aggregates.

For the systematically low fraction of 1–10 μm sized grains in the Encke Gap ringlets, the relevance of such moon-induced aggregation is far less clear. While the particles in all three Encke Gap ringlets periodically encounter the moon Pan either as they drift by the moon (for the inner and outer ringlets) or undergo horseshoe motion (for the central ringlet), it is not obvious whether these encounters could produce regions of reduced velocity dispersions like those predicted for the F ring. In the F ring, regions of reduced velocity dispersion and increased density occur due to the longitudinal variations in the perturbations to the ring particles' semi-major axes, which arise because of the epicyclic motion of Prometheus and the F ring relative to each other (Beurle et al., 2010). Since Pan is on a nearly circular orbit, similar longitudinal gradients in the semi-major axis shift cannot be produced within the Encke Gap by Pan's epicyclic motion. However, the Encke Gap ringlets, like the Charming Ringlet, exhibit some degree of heliotropic behavior, in which solar radiation pressure causes the geometrical center of the ringlet to be displaced from the center of Saturn towards the Sun (Hedman et al., 2007, 2010). Due to this forced eccentricity in the ring particles' orbits, particles encountering Pan at different longitudes relative to the Sun will be at different phases in their epicyclic motion. This should lead to longitudinal variations in the semi-major axis perturbations like those required to produce regions of enhanced density and reduced velocity dispersion. Such a model could potentially explain why the Encke Gap ringlets have distinctly different size distributions than the Charming Ringlet, whose gap is devoid of Pan-sized moons. However, a possible problem with this idea is that the Pan-induced perturbations on the different Encke ringlets have different strengths and occur on different timescales, so it is not clear if such perturbations would affect the size distributions of all three ringlets equally.

Of course, there are a number of other possible processes that might also be responsible for the observed variations in these rings' particle size distributions. For example, the overall dynamical environments the rings inhabit may influence how efficiently particles of different sizes are generated and how quickly particles are lost to the system by collisions with nearby rings and moons. In this context, the compact F-ring structures might correspond to regions where larger particles are produced more rapidly than other parts of the ring, perhaps again due to differences in the typical impact speeds into and between particles. Future detailed comparisons of these spectral data with predictions derived from various models of the relevant processes should yield useful new insights into the dynamics and particle properties of these dusty rings.

Acknowledgments

We wish to acknowledge NASA, the Cassini project and the VIMS team for providing the data that made this analysis possible. We also thank H. Throop and J.N. Cuzzi for their detailed and insightful reviews of this manuscript, and L. Esposito and C. Murray for the useful discussions. This work was supported in part by a Cassini Data Analysis Program Grant NNX09AE74G.

References

Arnott, W.P., Dong, Y.Y., Hallett, J., 1995. Extinction efficiency in the infrared (2–18 μm) of laboratory ice clouds: Observations of scattering minima in the Christiansen bands of ice. Appl. Opt. 34, 541–551.

Beurle, K., Murray, C.D., Williams, G.A., Cooper, N.J., Agnor, C.B., 2010. Direct evidence for gravitational instability and moonlet formation in Saturn's rings. Astrophys. J. 718, 176–180.

Bosh, A.S., Olkin, C.B., French, R.G., Nicholson, P.D., 2002. Saturn's F ring: Kinematics and particle sizes from stellar occultation studies. Icarus 157, 57–75.

Brown, R.H., Baines, K.H., Bellucci, G., Bibring, J.-P., Buratti, B.J., Capaccioni, F., Cerroni, P., Clark, R.N., Coradini, A., Cruikshank, D.P., 2004. The Cassini Visual and Infrared Mapping Spectrometer (VIMS) investigation. Space Sci. Rev. 115, 111–168.

Christiansen, C., 1884. Untersuchungen über die optischen Eigenschaften von fein vertheilten Körpern. Ann. Phys. Chem. 23, 298–306.

Christiansen, C., 1885. Untersuchungen über die optischen Eigenschaften von fein vertheilten Körpern. Ann. Phys. Chem. 24, 439–446.

Cuzzi, J.N., 1985. Rings of Uranus – Not so thick, not so black. Icarus 63, 312–316.

Cuzzi, J., Clark, R., Filacchione, G., French, R., Johnson, R., Marouf, E., Spilker, L., 2009. Ring particle composition and size distribution. In: Dougherty, M.K., Esposito, L.W., Krimigis, S.M. (Eds.), Saturn from Cassini–Huygens, pp. 459–509.

Dominik, C., Tielens, A.G.G.M., 1997. The physics of dust coagulation and the structure of dust aggregates in space. Astrophys. J. 480, 647–673.

Elachi, C., van Zyl, J., 2006. Introduction to the Physics and Techniques of Remote Sensing, second ed. John Wiley.

Esposito, L.W., Meinke, B.K., Colwell, J.E., Nicholson, P.D., Hedman, M.M., 2008. Moonlets and clumps in Saturn's F ring. Icarus 194, 278–289.

French, R.G., Nicholson, P.D., 2000. Saturn's Rings: II. Particle sizes inferred from stellar occultation data. Icarus 145, 502–523.

French, R.G., Nicholson, P.D., Porco, C.C., Marouf, E.A., 1991. Dynamics and structure of the Uranian rings. In: Bergstralh, J.T., Miner, E.D., Matthews, M.S. (Eds.), Uranus, pp. 327–409.

French, R.G., Nicholson, P.D., Cooke, M.L., Elliot, J.L., Matthews, K., Perkovic, O., Tollestrup, E., Harvey, P., Chanover, N.J., Clark, M.A., 1993. Geometry of the Saturn system from the 3 July 1989 occultation of 28 SGR and Voyager observations. Icarus 103, 163–214.

Güttler, C., Blum, J., Zsom, A., Ormel, C.W., Dullemond, C.P., 2010. The outcome of protoplanetary dust growth: Pebbles, boulders, or planetesimals? I. Mapping the zoo of laboratory collision experiments. Astro. Astrophys. 513, A56–+.

Hapke, B., 1993. Theory of Reflectance and Emittance Spectroscopy. Cambridge University Press.

Hedman, M.M., Burns, J.A., Tiscareno, M.S., Porco, C.C., 2007. The heliotropic rings of Saturn. Bull. Am. Astron. Soc. 38, 427.

Hedman, M.M., Nicholson, P.D., Salo, H., Wallis, B.D., Buratti, B.J., Baines, K.H., Brown, R.H., Clark, R.N., 2007. Self-gravity wake structures in Saturn's A ring revealed by Cassini VIMS. Astron. J. 133, 2624–2629.

Hedman, M.M., Burt, J.A., Burns, J.A., Tiscareno, M.S., 2010. The shape and dynamics of a heliotropic dusty ringlet in the Cassini Division. Icarus 210, 284–297.

Hedman, M.M., Nicholson, P.D., Baines, K.H., Buratti, B.J., Sotin, C., Clark, R.N., Brown, R.H., French, R.G., Marouf, E.A., 2010. The architecture of the Cassini Division. Astron. J. 139, 228–251.

Horányi, M., Burns, J.A., Hedman, M.M., Jones, G.H., Kempf, S., 2009. Diffuse rings. In: Dougherty, M.K., Esposito, L.W., Krimigis, S.M. (Eds.), Saturn from Cassini–Huygens. Springer, pp. 511–536.

Liou, K.N., Yang, P., Takano, Y., Sassen, K., Charlock, T., Arnott, W., 1998. On the radiative properties of contrail cirrus. Geophys. Res. Lett. 25, 1161–1164.

Mastrapa, R.M., Sandford, S.A., Roush, T.L., Cruikshank, D.P., Dalle Ore, C.M., 2009. Optical constants of amorphous and crystalline H_2O–ice: 2.5–22 μm (4000–455 cm^{-1}) optical constants of H_2O–ice. Astrophys. J. 701, 1347–1356.

Meinke, B.K., Esposito, L.W., Albers, N., 2010. UVIS ring occultations show F ring feature location and optical depth correlated with Prometheus. Bull. Am. Astron. Soc. 41, 939.

Murray, C.D., Beurle, K., Cooper, N.J., Evans, M.W., Williams, G.A., Charnoz, S., 2008. The determination of the structure of Saturn's F ring by nearby moonlets. Nature 453, 739–744.

Nicholson, P.D., Hedman, M.M., 2010. Self-gravity wake parameters in Saturn's A and B rings. Icarus 206, 410–423.

Prost, R., 1968. The influence of the Christiansen Effect on I.R. spectra of powders. Clays Clay Miner. 21, 363–368.

Showalter, M.R., Pollack, J.B., Ockert, M.E., Doyle, L.R., Dalton, J.B., 1992. A photometric study of Saturn's F Ring. Icarus 100, 394–411.

Vahidinia, S. et al., 2011. Saturn's F ring grains: Aggregates of crystalline water ice. Icarus, submitted for publication.

van de Hulst, H.C., 1957. Light Scattering by Small Particles. John Wiley and Sons, New York.

Wada, K., Tanaka, H., Suyama, T., Kimura, H., Yamamoto, T., 2009. Collisional growth conditions for dust aggregates. Astrophys. J. 702, 1490–1501.